Acta Pharmaceutica Sinica B 2024;14(8):3711−3729

Chinese Pharmaceutical Association
Institute of Materia Medica, Chinese Academy of Medical Sciences

Acta Pharmaceutica Sinica B

www.elsevier.com/locate/apsb
www.sciencedirect.com

ORIGINAL ARTICLE

CCL9/CCR1 axis-driven chemotactic nanovesicles for attenuating metastasis of SMAD4-deficient colorectal cancer by trapping TGF-β

Boning Niu [a,†], Tianyi Tian [a,†], Lu Wang [b,†], Yinmei Tian [a], Tian Tian [a], Yuanyuan Guo [c], Hu Zhou [d], Zhiping Zhang [a,e,f,*]

[a]*Tongji School of Pharmacy, Huazhong University of Science and Technology, Wuhan 430030, China*
[b]*Department of Oncology, Tongji Hospital, Tongji Medical College, Huazhong University of Science and Technology, Wuhan 430030, China*
[c]*Department of Pharmacy, Liyuan Hospital, Tongji Medical College, Huazhong University of Science and Technology, Wuhan 430030, China*
[d]*School of Pharmaceutical Sciences, Fujian Provincial Key Laboratory of Innovative Drug Target Research, High Throughput Drug Screening Platform, Xiamen University, Xiamen 361102, China*
[e]*National Engineering Research Center for Nanomedicine, Huazhong University of Science and Technology, Wuhan 430030, China*
[f]*Hubei Engineering Research Centre for Novel Drug Delivery System, Huazhong University of Science and Technology, Wuhan 430030, China*

Received 16 January 2024; received in revised form 9 April 2024; accepted 15 April 2024

KEY WORDS

SMAD4-deficient CRC;
Metastasis;
G-MDSCs;
TGF-β;
CCR1;
TGFBR2;

Abstract SMAD4 deficiency in colorectal cancer (CRC) is highly correlated with liver metastasis and high mortality, yet there are few effective precision therapies available. Here, we show that CCR1$^+$-granulocytic myeloid-derived suppressor cells (G-MDSCs) are highly infiltrated in SMAD4-deficient CRC *via* CCL15/CCR1 and CCL9/CCR1 axis in clinical specimens and mouse models, respectively. The excessive TGF-β, secreted by tumor-infiltrated CCR1$^+$-G-MDSCs, suppresses the immune response of cytotoxic T lymphocytes (CTLs), thus facilitating metastasis. Hereby, we develop engineered nanovesicles displaying CCR1 and TGFBR2 molecules (C/T-NVs) to chemotactically target the tumor

*Corresponding author.
E-mail address: zhipingzhang@mail.hust.edu.cn (Zhiping Zhang).
†These authors made equal contributions to this work.
Peer review under the responsibility of Chinese Pharmaceutical Association and Institute of Materia Medica, Chinese Academy of Medical Sciences.

https://doi.org/10.1016/j.apsb.2024.05.009

Chemotactic nanovesicles; Tertiary lymphoid structures

driven by CCL9/CCR1 axis and trap TGF-β through TGF-β-TGFBR2 specific binding. Chemotactic C/T-NVs counteract CCR1$^+$-G-MDSC infiltration through competitive responding CCL9/CCR1 axis. C/T-NVs-induced intratumoral TGF-β exhaustion alleviates the TGF-β-suppressed immune response of CTLs. Collectively, C/T-NVs attenuate liver metastasis of SMAD4-deficient CRC. In further exploration, high expression of programmed cell death ligand-1 (PD-L1) is observed in clinical specimens of SMAD4-deficient CRC. Combining C/T-NVs with anti-PD-L1 antibody (aPD-L1) induces tertiary lymphoid structure formation with sustained activation of CTLs, CXCL13$^+$-CD4$^+$ T, CXCR5$^+$-CD20$^+$ B cells, and enhanced secretion of cytotoxic cytokine interleukin-21 and IFN-γ around tumors, thus eradicating metastatic foci. Our strategy elicits pleiotropic antimetastatic immunity, paving the way for nanovesicle-mediated precision immunotherapy in SMAD4-deficient CRC.

1. Introduction

Colorectal cancer (CRC) develops through the accumulation of genetic alterations in oncogenes and tumor suppressor genes, including APC, TP53, and SMAD4[1]. SMAD4 deficiency is observed in 30%−40% of colorectal cancer (CRC) patients and is highly correlated with colorectal cancer liver metastasis (CRLM), which is the predominant cause of CRC-related death[2−4]. SMAD4 is a common SMAD (co-SMAD) mediating the transforming growth factor-β (TGF-β) signaling pathway[5,6]. In the canonical TGF-β signal transduction, TGF-β binds to the type II receptor (TGFBR2) and then recruits and activates the type I receptor (TGFBR1) on the plasma membrane thus activating TGFBRI. Activated TGFBRI phosphorylates receptor-activated R-SMADs (SMAD2 and SMAD3), leading to their association with SMAD4 to form the R-SMADs/SMAD4 complex that translocates into the nucleus and binds DNA elements to regulate gene transcription[7]. SMAD4 deficiency inactivates canonical TGF-β signaling and induces numerous cell-autonomous changes[8−10]. We previously reported that SMAD4 deficiency induced the alteration of the inhibitor of differentiation-1, which promoted tumor cell stemness and chemoresistance to oxaliplatin[11,12]. Moreover, SMAD4 deficiency was associated with the high expression of programmed cell death ligand 1 (PD-L1) and tumor cell immune escape[8].

In addition to the cell-autonomous changes, accumulating evidence indicates that tumor-associated stromal cells play critical roles in the metastatic progression of SMAD4-deficient CRC[13,14]. Myeloid-derived suppressor cells (MDSCs) are the major stromal constituents that suppress the function of other immune cells by creating a suppressive microenvironment in the tumor stroma[15]. It has been reported that loss of SMAD4 induces increased expression of the chemokine factor CCL15, recruiting CCR1$^+$-MDSCs *via* the CCL15/CCR1 axis to metastatic foci in the progression of human CRC malignancy[3,16−18]. Blockade of the CCL15/CCR1 axis is regarded as an attractive target for the treatment of autoimmune and cancer[19,20]. Nevertheless, the underlying metastatic mechanism of CCR1$^+$-MDSCs is still unclear. MDSCs are heterogeneous populations of immature myeloid cells that comprise granulocytic (G-MDSC) and monocytic (M-MDSC) subsets, both of which have been found to exhibit immunosuppressive properties[21,22]. However, G-MDSCs and M-MDSCs subsets have distinct gene expression profiles[23]. Thus, characterizing which subset of MDSCs plays the dominant role in SMAD4-deficient CRC metastatic progression is an urgent problem to be solved in clinical antitumor therapy.

TGF-β, a tumor-promoting factor, counteracts immune responses by impacting the proliferation and differentiation of multiple immune cells and ultimately maintains the immunosuppressive microenvironment[24,25]. Notably, TGF-β directly suppresses the cytotoxicity program of CD8$^+$ cytotoxic T lymphocytes (CTLs) by downregulating the expression of granzymes B[26]. In a similar effect, TGF-β induces Foxp3 expression and generates CD4$^+$CD25$^+$ regulatory T cells (Tregs), which counteract the immune response of CTLs[27,28]. In addition, exogenous administration of TGF-β suppresses B-cell proliferation[29]. TGF-β also exerts a significant impact on the myeloid lineage, such as the maturation of G-MDSCs[30]. Thus, neutralization of TGF-β exerts a potent antitumor effect in several clinical trials[31]. However, the various pathological functions of TGF-β are tumor-specific and related to the infiltration of immune cells[30]. Marked changes in the cell phenotype and immune cell infiltration were observed in SMAD4-deficient CRC[32]. Hence, whether inhibiting TGF-β signaling is an effective treatment in SMAD4-deficient CRC needs to be elucidated.

In this study, we demonstrated that SMAD4 deficiency led to the recruitment of CCR1$^+$-G-MDSCs *via* the CCL15/CCR1 and CCL9/CCR1 axis in clinical specimens and mouse models, respectively. CCR1$^+$-G-MDSCs showed a dominant promigratory effect by producing excessively abundant TGF-β, which impaired the immune response of CTLs. Subsequently, engineered nanovesicles displaying CCR1 and TGFBR2 (C/T-NVs) were developed and exhibited favorable therapeutic efficacies by counteracting the accumulation of CCR1$^+$-G-MDSCs, decreasing intratumorally excessive TGF-β molecules and trapping essential TGF-β molecules. C/T-NV-mediated TGF-β inhibition resulted in a significantly high recruitment rate of tumor-infiltrated CTLs and attenuated spontaneous liver metastasis of SMAD4-deficient CRC in the mouse model. In addition, we revealed that SMAD4 deficiency led to abnormal upregulation of PD-L1 in clinical specimens. C/T-NVs were further combined with anti-PD-L1 antibody (aPD-L1), a known agent used for immune checkpoint blockade. Surprisingly, the combination of C/T-NVs and aPD-L1 facilitated the formation of tertiary lymphoid structures (TLSs) around the tumor, contributing to the sustained activation of CTLs, CXCL13$^+$ T and CXCR5$^+$ B cells, enhanced expression of cytokine interleukin-21 (IL21) and IFN-γ and eradicated metastatic foci (Scheme 1). This study revealed the metastatic mechanism of

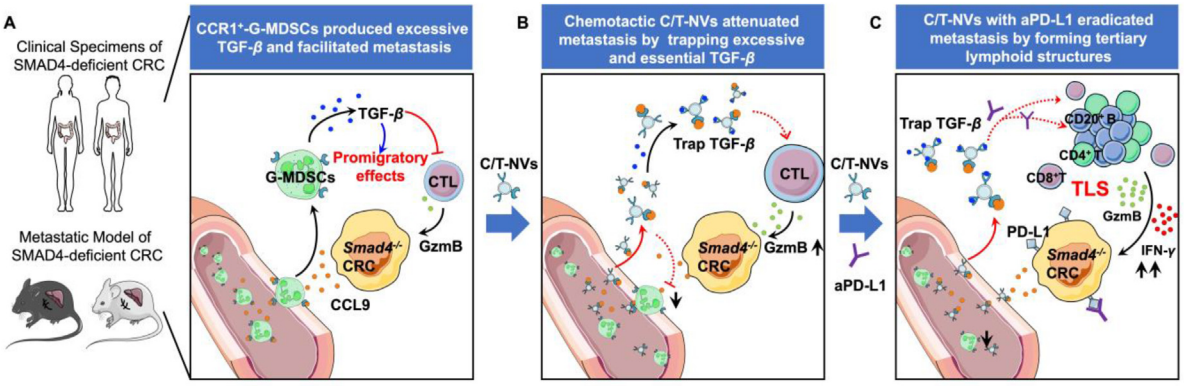

Scheme 1 Schematic illustration of chemotactic C/T-NVs as a pleiotropic therapeutic strategy to eliminate metastasis SMAD4-deficient colorectal cancer. (A) SMAD4-deficient colorectal cancer cells ectopically express chemokine CCL9 and recruit CCR1$^+$-G-MDSCs to metastatic foci *via* the CCL9/CCR1 axis in the mouse model. CCR1$^+$-G-MDSCs produce excessive abundant TGF-β which directly inhibits the activity of CTLs and promotes metastasis. (B) C/T-NVs chemotactically target metastatic foci driven by the CCL9/CCR1 axis and counteract the accumulation of CCR1$^+$-G-MDSCs, thus suppressing CCR1$^+$-G-MDSCs-derived TGF-β. Tumor-infiltrated C/T-NVs trap excessive and essential TGF-β, thus leading to the activation of CTLs and attenuating metastasis of SMAD4-deficient CRC. (C) The combination of C/T-NVs and aPD-L1 facilitates the formation of TLSs around metastatic foci, contributing to the sustained activation of CTLs and release of cytotoxic IFN-γ and GzmB, and eradicates SMAD4-deficient CRC.

MDSC infiltration-related metastasis of SMAD4-deficient CRC and demonstrated pleiotropic immunotherapy based on engineered nanovesicles.

2. Materials and methods

2.1. Cell culture

HEK293 cell line and CT26 colon cancer line were purchased from American Type Culture Collection (ATCC), and the MC38 colon cancer cell line was purchased from the Cell Bank of Chinese Academy of Science (Shanghai, China). HEK293 and MC38 were cultured in Dulbecco's modified Eagle's medium (DMEM) supplemented with 10% fetal bovine serum (FBS) and 100 U/mL penicillin-streptomycin. CT26 cells and sorted intratumoral CCR1$^+$-MDSCs were cultured in RPIM 1640 supplemented with 10% FBS and 100 U/mL penicillin-streptomycin. All cell lines were cultured in a humidifying atmosphere under 5% CO_2 at 37 °C.

2.2. The construction of stable cell lines

MC38 stable cell lines were constructed by lentivirus. Plasmids encoding CCR1 or TGFBR2 (pLenti-GFP/puro-CCR1 and pLenti-RFP/puro-TGFBR2) were purchased from Genomeditech (Shanghai, China). Briefly, HEK293 cells were transfected with target plasmids and helper plasmids pMDL, VSVG, and pRSV-Rev using Lipofectamine 2000 transfection reagent (Thermo Fisher, Cat# 11668019). After 48 h, the cell supernatants containing lentiviruses were harvested through 0.45 μm filters. MC38 cells were infected with lentiviral supernatants and polybrene (Yeasen, Cat# 40804ES76) for 48 h, and then selected with puromycin (Yeasen, Cat# 60210ES60) at the dose of 10 μg/mL for 1 week. The puromycin-resistant cells were harvested and flow-cytometric sorted of GFP or RFP positive cells into a sterile 96-well plate using Flow Cell Sorter (MA900, SONY, Japan).

2.3. Preparation of NVs

Engineered NVs were constructed by membrane extrusion. Briefly, the corresponding engineered cells were digested with 0.25% (*w/v*) trypsin and centrifuged at 400×*g* for 5 min (Hunan Xiangyi Laboratory Instrument Development Co., Ltd., China). Collected the cell pellet and washed with HBSS. Then resuspended 2×10^7 cells with 1 mL pre-cooled Membrane and Cytosol Protein Extraction Kit A (Beyotime, Cat# P0033-1) containing 1 mmol/L PMSF and incubated for 15 min at 4 °C. The cell suspension was transferred to the pre-cooled Dounce and homogenized 50 times, followed by centrifugation at 700×*g* for 10 min at 4 °C to remove cell nuclei. The collected supernatant was incubated with the 20 μg/mL DNase at 37 °C for 30 min and then centrifuged at 700×*g* for 10 min at 4 °C to discard the remaining debris. The supernatant was centrifuged at 14,000×*g* for 1 h to precipitate the cell membrane. For NVs fabrication, the dissolved membrane was diluted with HBSS and extruded five times *via* 1 μm polycarbonate membrane filters. Finally, the extruded sample was centrifugated at 14,000×*g* for 1 h to collect NVs.

2.4. Characterisation of NVs

The hydrated size and Zeta potential of NVs were analyzed by dynamic light scattering (DLS, Brookhaven Instruments, NY, USA) and nanoparticle tracking analysis (NTA, NanoSight, Malvern Panalytical, Shanghai, China), respectively. The solution of NVs was diluted and applied to a NanoSight LM10 (Malvern Panalytical) chamber and analyzed by NTA v3.0 0068 software. Three recordings of nanoparticle tracking analysis (NTA, NanoSight, Malvern Panalytical) using a SCMOS camera for each sample and were analyzed by NTA v3.0 0068 software. For transmission electron microscopy (TEM) observation, the collected NVs were suspended in HBSS and fixed by 4% paraformaldehyde for 30 min. Subsequently, 10 μL NVs solution was placed on formvar carbon-coated copper grids and settled for 30 min. After staining with 2% (*w/v*) uranyl acetate and air-drying,

grids were observed under TEM (HITACHI HT7800, Japan) at 80 kV. The protein molecules on the NVs surface were analyzed by immunogold transmission electron microscopy (IG-TEM) as previously reported by Jan et al.[33] with minor modifications. Briefly, NVs suspended in HBSS were placed on carbon-coated copper grids, blocked, and incubated with TGFBR2 antibody (1:50, Absin, Cat# abs148273), CCR1 antibody (1:50, Abclonal, Cat# A18341) or TGF-β1 (1:50, Abclonal, Cat# A16640) for 2 h at room temperature, followed by incubation with CMC-Protein A-gold (colloidal gold 10 nm, 1:20, Cell Microscopy Core, Department of Cell Biology, University Medical Center Utrecht) for 30 min at room temperature. Each staining step was washed with PBS with 0.1% BSA. At last, colloidal gold labeled NVs were fixed with 1% glutaraldehyde (*w*/*v*) in PBS before contrast staining with 2% (*w*/*v*) uranyl acetate. The gold-labeled NVs were observed under the TEM (HITACHI HT7800) at 80 kV.

2.5. Animal study and spontaneous liver metastasis of CRC

Mice experiments were approved by the Institutional Animal Care and Use Committee of Huazhong University of Science and Technology, with the assigned [2021] IACUC number (3380). BALB/c (female, 6−8 weeks, 18−20 g) and C57BL/6 (female, 6−8 weeks, 18−20 g) mice were purchased from China Three Gorges University (Yichang, China). All mice were kept under specific pathogen-free conditions in the Laboratory Animal Center of Huazhong University of Science and Technology and housed at temperatures of 21−23 °C, humidity of 50%−55% in a 12-h light/dark cycle, with free access to standard food and water. For the spontaneous metastasis model, cells were digested by 0.25% trypsin without EDTA and resuspended in saline at a 5×10^6 cells/mL density. Mice aged 6−8 weeks were anesthetized with isoflurane by inhaling *via* RWD isoflurane R580 (RWD, Shenzhen, China) and placed on a warm, sterilized operating table. A left flank incision was made below the edge of the rib to expose the abdominal cavity, and the spleen was revealed by gentle pressing on the abdomen. 100 μL cell suspension was slowly injected into the splenic pulp through a 26-gauge needle over 1 min, followed by stanching with sterilized cotton for 3 min. For the galunisertib treatment, mice with MC38 intrasplenic injection received intragastric administration of galunisertib (75 mg/kg) (MCE, Cat# HY-13226) or vehicle control daily for 7 days. For NV intervention, the ctr-NVs, C-NVs, T-NVs, and C/T-NVs were administered every 2 days for 4 times at a dose of 5E11 count (i.v.) in the spontaneous spleen metastasis model mice with MC38 or MC38-luc intrasplenic injection. For the combination of NVs and aPD-L1, mice with MC38 intrasplenic injection were treated with HBSS vehicle, ctr-NVs, ctr-NVs+aPD-L1, C/T-NVs, C/T-NVs+aPD-L1. Ctr-NVs or C/T-NVs were administered on Days 1, 3, 5, and 7 post-tumor injection at a dose of 5E11 count (i.v.). aPD-L1 (Bio X cell, clone 10F.9G2, Cat# BE0101) was administered on Days 2, 5, and 8 post-tumor injection at a dose of 100 μg per mouse. On Day 14, the orbital blood samples of mice were collected and centrifuged at 400×*g* for 15 min to collect serum for further cytokine analysis by ELISAs. Mice were sacrificed, and the spleens and livers were excised and weighed. Analysis of liver coefficient (liver weight/body weight) to evaluate the tumor growth and metastasis level. Fresh tumor sections were digested to prepare single-cell suspension for further FACS analysis. Tumors with adjacent tissues were fixed by 4% paraformaldehyde and used for hematoxylin-eosin (H&E) and immunohistochemistry (IHC) staining. Other tumor sections were homogenized in TNT buffer (Beyotime, Cat# P0013) supplemented with protease inhibitor cocktails (Roche, Cat# 4693124001) for Western blot analysis. For the survival curve, the number of dead mice was counted daily within 60 days after the tumor inoculation. Based on the results, the survival curves were shaped using GraphPad Prism 9.0 software.

2.6. Western blot

Cell and NV lysates were prepared using TNT buffer containing a complete protease inhibitor cocktail. Mice tumor samples were mechanically homogenized using a homogenizer (Tissuelyser-24, Shanghai Jingxin Experimental Technology, Shanghai, China) in TNT buffer containing a complete protease inhibitor cocktail. Lysates were centrifuged at 18,000×*g* for 15 min at 4 °C and protein concentrations of supernatants were determined by Pierce BCA Protein Assay Kit (Thermo Fisher, Cat# 23225) according to the manufacturer's instructions. Then, samples containing an equal amount of protein were boiled in 6 × Loading buffer for 10 min at 100 °C, resolved by 8%−15% SDS-polyacrylamide gel electrophoresis and transferred to nitrocellulose membrane (Pall Corporation, Cat# 66485). The nitrocellulose membranes were blocked in 5% milk in TBS for 1 h at room temperature, and subsequently incubated with appropriate primary antibodies at 4 °C overnight and probed with DyLight™ 800 4× PEG-Conjugate secondary antibodies (Cell Signaling Technology, Cat# 5151 and 5257) for 1 h at room temperature. Protein bands were visualized using Odyssey DLx Imaging System (LI-COR, USA), and the Image J software was applied to quantify the intensity of protein bands. Primary antibody. CCR1 (1:1000, Abclonal, Cat# A18341), TGFBR2 (1:1000, Absin, Cat# abs148273), GAPDH (1:1000, Santa Cruz, Cat# sc-365062), Na^+/K^+-ATPase (Santa Cruz, Cat# sc-21712), SMAD2 (1:1000, CST, Cat# 5339), p-SMAD2 (1:1000, CST, Cat# 18338), SMAD4 (1:1000, Santa Cruz, Cat# sc-7966).

2.7. MDSC depletion

MC38 and CT26 cells were injected into the spleens of C57/BL6 and BALB/c mice, respectively. To deplete MDSC, mice were injected intraperitoneally with 200 μg anti-Gr1 (clone RB6-8C5, Biolegend, Cat# 108454) or isotype (clone RTK4530, Biolegend, Cat# 400672) every three days. Mice were sacrificed on Day 14 after the tumor injection, and livers were excised. Tumor sections from livers were harvested and digested into single-cell suspension, followed by further FACS analysis.

2.8. Peripheral blood mononuclear cell (PBMC) isolation

Peripheral blood samples were provided by the Pathology Department of Tongji Hospital. Human blood samples from human subjects were approved by the Medical Ethics Committee of Tongji Medical College, with the assigned [2015] S003. All samples obtained were approved by TRIAL REGISTRATION, ClinicalTrials.gov, identifier: NCT02717923. PBMC was isolated from Peripheral blood *via* Lymphoprep™ (Serumwerk Bernburg AG, Cat# 1856) in accordance with the manufacturer's instructions. Briefly, dilute the blood 1:1 with 0.9% NaCl solution, followed by carefully layering 6 mL of the diluted blood over 3 mL Lymphoprep™ in a 15 mL centrifuge tube. Then, the gradients were centrifuged at 800×*g* for 20 min at 20 °C in a swinging-bucket rotor. The PBMC interface was carefully

removed using a Pasteur pipette without removing the upper layer. Lastly, the harvested fraction was diluted with 0.9% NaCl solution to reduce the density of the resolution, followed by centrifugation at 250×*g* for 10 min to collect PBMC.

2.9. Flow cytometry analysis

For analysis of immunocytes in tumors from indicated mice metastatic tissues. The tumor sections were harvested and digested with 1 mg/mL type IV collagenase (BioFroxx, Cat# 2091), 0.1 mg/mL DNase (Shanghai yuanye Bio-Technology Co., Ltd., Cat# S10073) and 0.1 mg/mL hyaluronidase (BioFroxx, Cat# 1141MG100) at 37 °C for 90 min. The suspension was filtered by the 70 μm strainer and centrifuged at 400×*g* for 5 min to collect the cells, followed by incubation with red blood cell lysis buffer (Solarbio, Cat# R1010) to prepare the single-cell suspension. Cells were stained with BD Horizon™ Fixable Viability Stain 700 (1:1000, BD Biosciences, Cat# 564997) for staining of dead cells and blocked Fc nonspecific binding by anti-CD16/32 antibody (1:100, clone 93, Biolegend, Cat# 101302) for 15 min. For analysis of mouse MDSCs population, cells were stained with anti-CD45 PerCP-Cy5.5 (1:100, clone 30-F11, Biolegend, Cat# 103132), anti-CD11b FITC (1:100, clone M1/70, Biolegend, Cat# 101206), anti-Ly6G PE (1:100, clone 1A8, BD Biosciences, Cat# 551461), anti-Ly6C APC (1:100, clone HK1.4, Biolegend, Cat# 128016), anti-CCR1 PE-Cy7 (1:100, clone S15040E, Biolegend, Cat# 152509). For analysis of mouse B cells population, cells were stained with anti-CD45 PerCP-Cy5.5 (1:100, clone 30-F11, Biolegend, Cat# 103132), anti-CD45R/B220 PE (1:100, clone RA3-6B2, BD Biosciences, Cat# 553090), anti-CD80 APC (1:100, clone 16-10A1, BD Biosciences, Cat# 560016), anti-Mouse MHC Class II (I-A/I-E) FITC (1:100, clone 2G9, BD Biosciences, Cat# 553623), anti-CD69 PE-Cy7 (1:100, clone H1.2F3, BD Biosciences, Cat# 552879). For analysis of mouse Treg and $GzmB^+$ cells population, cells were first stained with anti-CD45 PerCP-Cy5.5 (1:100, clone 30-F11, Biolegend, Cat# 103132), anti-CD3 BV510 (1:100, clone 17A2, Biolegend, Cat# 100234), anti-CD4 FITC (1:100, clone GK1.5, Biolegend, Cat# 100406), anti-CD8a BV421 (1:100, clone 53−6.7, Biolegend, Cat# 100738), anti-CD69 PE-Cy7 (1:100, clone H1.2F3, BD Biosciences, Cat# 552879), anti-CD25 PE (1:100, clone PC61, Biolegend, Cat# 102008), fixed and permeabilized with True-Nuclear™ Transcription Factor Buffer Set (BioLegend, Cat# 424401), and finally stained with anti-Granzyme B PE/Dazzle 594 (1:100, clone QA16A02, BioLegend, Cat# 372216), anti-Foxp3 AF647 (1:100, clone MF-14, BioLegend, Cat# 126408) in accordance with the manufacturer's instructions.

For analysis of the human MDSCs population in PMBC from clinical patients, the isolated PBMC was stained with BD Horizon™ Fixable Viability Stain 700 for 10 min and blocked by Human BD Fc BlockTM (1:100, clone Fc1, BD Biosciences, Cat# 564220) for 15 min. Then cells were stained with anti-CD3 PerCP-Cy5.5 (1:20, clone UCHT1, BD Biosciences, Cat# 560835), anti-CD19 PerCP-Cy5.5 (1:20, clone HIB19, BD Biosciences, Cat# 561295), anti-CD56 PerCP-Cy5.5 (1:20, clone B159, BD Biosciences, Cat# 566400), anti-CD11 b PE (1:100, clone M1/70, BD Biosciences, Cat# 557397), anti-HLA-DR FITC (1:5, clone G46-6, BD Biosciences, Cat# 555811), anti-CD33 APC (1:5, clone WM53, BD Biosciences, Cat# 551378), anti-CD45 APC-Cy7 (1:20, clone 2D1, BD Biosciences, Cat# 557833), anti-CD14 BV605 (1:20, clone M5E2, BD Biosciences, Cat# 564054), anti-CD15 V450 (1:20, clone HI98, BD Biosciences, Cat# 561584) and anti-CD191 (CCR1) PE-Cy7 (1:20, clone 5F10B29, BioLegend, Cat# 362914). All samples were analyzed with Sony ID7000 spectral cell analyzer (Sony). FACS data were analyzed with FlowJo v10.4.

2.10. Immunohistochemistry

Formalin-fixed and paraffin-embedding samples from clinical patients were provided by Pathology Department of Tongji Hospital and cut into slices as thin as 5 μm by a microtome slicer (Leica, Germany). All samples obtained were approved by TRIAL REGISTRATION, ClinicalTrials.gov, identifier: NCT02717923. The paraffin-embedded slices were gradually deparaffinized by xylene and ethanol according to standard protocols and boiled by microwave for epitope retrieval in sodium citrate buffer (1.8 mmol/L citric acid and 8.2 mmol/L sodium citrate in PBS)[34]. The sections were processed by 3% H_2O_2 in methanol for 30 min in the dark to quench endogenous target activity. Incubated with glycine (0.1 mol/L in PBS) and 5% goat serum (Zsbio, Cat# ZLI-9056) for 1 h at room temperature. The sections were incubated with primary antibodies, which were diluted at a ratio of 1:100 in 1% BSA overnight at 4 °C, followed by incubation with secondary antibodies (Zsbio, Cat# PV-9002 and Cat# PV-9001). Finally, the sections were processed with DAB (Zsbio, Cat# ZLI-9017) for 1 min, gradually dehydrated with xylene and ethanol and sealed with neutral balsam (Macklin, Cat# N861409). Primary antibodies: SMAD4 (Santa Cruz, Cat# sc-7966), CCR1 (Abclonal, Cat# A18341), CCL9 (Santa Cruz, Cat# sc-74228), p-SMAD2 (Absin, Cat# abs155124) and TGF-β1 (Abclonal, Cat# A16640). CD33, CD3, CD4, CD20, CD8, Ki67, and IFN-γ staining assays were served by Servicebio (Hubei Wuhan, China). Liver metastasis of MC38-tumor-bearing mice was fixed in 4% paraformaldehyde overnight at 4 °C. The graded ethanol and xylene dehydrated the tissues for preservation and IHC analysis. After dehydration, the tissues were embedded in paraffin wax by a tissue embedding device (Leica). Subsequently, the paraffin-embedded tissues were cut into 5-μm-thick slices and then mounted onto glass slides.

2.11. Biodistribution of NVs

C57/BL6 mice with MC38 cells intrasplenic injection were intravenously administered with 0.5 mg/kg free DiR (MCE, Cat# HY-D1048) or 5E11 count of DiR labeled ctr-NVs, C-NVs, T-NVs and C/T-NVs (at an equal DiR dosage of 0.5 mg/kg), or 5E11 count of PKH26 labeled NVs. At 4 or 24 h after administration, the liver, spleen, and tumor sections were harvested from liver metastasis. The distribution of DiR-labeled NVs in tumors was investigated *via* the near-infrared fluorescence system (Pearl Trilogy, LI-COR, USA). The relative fluorescence intensities of the tumor sections, liver, and splenic tumors were quantified using the image studio v5.2.5. The distribution of PKH26 labeled NVs in tumors was imaged using confocal microscopes (AX, Nikon, Tokyo, Japan).

2.12. Bioluminescent reporter imaging

The development of metastasis was monitored every three days by bioluminescent reporter imaging. In more detail, intraperitoneal injection of D-Luciferin (Yeasen, Cat# 40902ES03) DPBS solution at a 150 mg/kg dosage at the indicated time. The *in vivo*

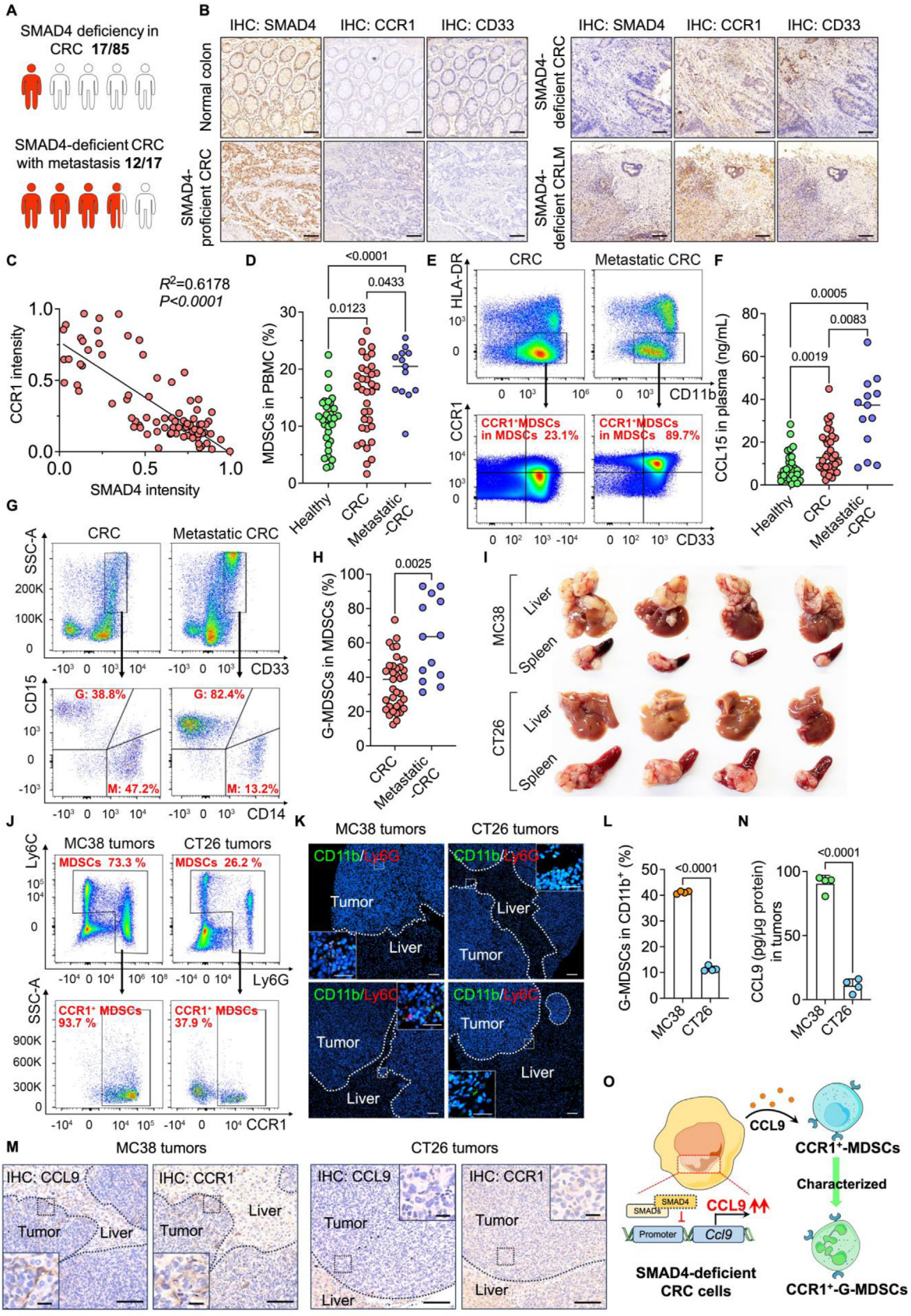

Figure 1 CCR1^{+}-G-MDSCs accumulate to SMAD4-deficient CRC tissues *via* the CCL15/CCR1 axis and CCL9/CCR1 axis in clinical specimens and mouse models. (A) Clinical specimens of human CRC were examined using immunohistochemistry staining for SMAD4, CCR1 and CD33, and (B) representative images of indicated specimens. Scale bar = 100 μm. (C) Immunohistochemistry analysis of human CRC

fluorescence imaging was performed using the IVIS system (IVScope 8000, CLINX, Shanghai, China) after 15 min of D-Luciferin injection. The fluorescence intensities were analyzed with Clinx IVScopeEQ Capture software.

2.13. Enzyme-linked immunosorbent assay (ELISA) and the expression ratio of CCR1 and TGFBR2

The blood was centrifuged at 1000×*g* for 20 min at 4 °C to obtain plasma. Mice tumor samples were mechanically homogenized using a homogenizer (Tissuelyser-24, Shanghai Jingxin Experimental Technology) in TNT buffer containing a complete protease inhibitor cocktail. The concentrations of CCL15 in the plasma of patients or healthy subjects were measured by Human CCL15 ELISA KIT (Solarbio, Cat# SEKH-0248). The concentrations of CCL9 of mice were measured by Mouse CCL9/10/MIP-1γ ELISA KIT (Solarbio, Cat# SEKM-0236). The concentrations of TGF-β1 were measured by Mouse TGF-β1 ELISA KIT (Solarbio, Cat# SEKM-0035). For activation of TGF-β1, the plasma was incubated with 1 mol/L HCl for 60 min at 4 °C followed by neutralization with 1 mol/L NaOH. The expression ratio of CCR1 and TGFBR2 in C/T-NVs were quantified using Mouse CCR1 ELISA KIT (FANKEW, Cat# F0101-MB) and Mouse TGFBR2 ELISA KIT (FANKEW, Cat# F0106-MB), respectively as previously reported[35]. All ELISA kits were carried out in accordance with the manufacturer's instructions.

2.14. Immunofluorescence

Indicated stable cells were seeded on in 24-well plates with 14 mm × 14 mm glass slides and then permeabilized with PBS containing 0.1% Triton X-100 and 0.1 mol/L glycine for 15 min and blocked with 1% BSA in PBS for 30 min at room temperature, followed with incubation with indicated primary TGFBR2 antibody (1:100, Absin, Cat# abs148273) or CCR1 antibody (1:100 Abclonal, Cat# A18341) at room temperature for 3 h and incubated with Cy5-labeled secondary antibody (Beyotime, Cat# A0468) at room temperature for 1 h. Cells were stained with DAPI (Sigma−Aldrich, Cat# D9542) and were imaged using confocal microscopes (AX, Nikon). For immunofluorescence staining of tissue slices, deparaffinized tumor tissues from liver metastasis were stained with primary antibody CXCR5 (1:50, Abclonal, Cat# A8950) and CXCL13 (1:50, Absin, Cat# abs125207) and Cy3-labeled secondary antibody (Beyotime, Cat# A0516) and DAPI. CD11b, Ly6C, and Ly6G staining assays were served by Servicebio (Hubei Wuhan, China).

2.15. Chemotaxis of CCR1-engineered cells and NVs

Chemotactic response assays for cells were determined using HTS Transwell-24 with 3 μm pores (Corning, Cat# 3398). Briefly, the slide was placed on the bottom chamber and indicated $CCR1^+$ cells or $CCR1^-$ cells were seeded in the top chamber. The indicated medium supplemented with or without CCL9 (10 ng/mL) was carefully added to the bottom chamber, followed by culturing for 48 h at 37 °C and 5% CO_2. Removed the insert and washed the slide twice with PBS. The migratory cells on the slide were fixed with 4% paraformaldehyde, stained with crystal violet solution (Beyotime, Cat# C0121) for 10 min at room temperature, washed with ddH_2O, and photographed.

Engineered NVs actively targeting $CCR1^+$ cells were determined using HTS Transwell-24 with 0.4 μm pores (Corning, Cat# 3396). Briefly, MC38 cells were seeded on a slide placed in the bottom chamber and cultured for 2 days. DiO-NVs were added into the top chamber and incubated for 6 h at 37 °C and 5% CO_2. The slides were washed twice with PBS, fixed with 4% paraformaldehyde, stained with DAPI, and observed under confocal microscopes (AX, Nikon).

Engineered NVs inhibiting $CCR1^+$ cells chemotaxis toward CCL9 was determined using HTS Transwell-24 with 3 μm pores (Corning, Cat# 3398). Briefly, the slide was placed on the bottom chamber, and $CCR1^+$ cells or sorted $CCR1^+$-MDSCs were seeded in the top chamber. The medium supplemented with indicated NVs and CCL9 (10 ng/mL) was added to the bottom chamber, followed by incubating for 48 h at 37 °C and 5% CO_2. Removed the insert and washed the slide twice with PBS. The migratory cells on the slide were fixed with 4% paraformaldehyde, stained with crystal violet solution for 10 min at room temperature, washed with ddH_2O, and photographed.

2.16. Real-time quantitative reverse transcription-PCR

Total RNA was isolated from tissue using TRIeasy™ Total RNA Extraction Reagent TRIeasy™ (Yeasen, Cat# 10606ES60) in accordance with the manufacturer's instructions. 1 μg total RNA was reverse transcribed into cDNA *via* Hifair™ II 1st Strand cDNA Synthesis SuperMix (Yeasen, Cat# 11120ES60) in accordance with the manufacturer's instructions. Real-time PCR was conducted using Hieff® qPCR SYBR Green Master Mix (Yeasen, Cat# 11202ES03) and AriaMx machine (Agilent, CA, USA). Expression levels of the target gene were normalized to *Gapdh* using the $2^{-\Delta\Delta CT}$ method. The designed primers (Sangon Biotech, Shanghai, China) were used for the following genes:

specimens showing the correlations of SMAD4 and CCR1 expression. Pearson correlation analysis was used to indicate correlation. (D) Fluorescence Activated Cell Sorter (FACS) analysis of the percent of MDSCs in PBMC from healthy subjects and clinical patients with CRC. (E) Representative FACS plots of $CD33^+$ $CCR1^+$ in $CD11b^+$ $HLA\text{-}DR^-$ cells. (F) Quantification of CCL15 concentration in plasma from healthy subjects and clinical patients with CRC. (G) Representative FACS plots and (H) quantification of the percent of $CD14^-$ $CD15^+$ (G-MDSCs) in MDSCs, respectively. G: G-MDSCs, M: MDSCs. (I) MC38 or CT26 cells were injected into spleens of C57BL/6 or BALB/c mice respectively. Mice were reared for 14 days and sacrificed for analysis of liver metastasis, $n = 4$. (J) Representative FACS plots of MDSCs in $CD11b^+$, $CCR1^+$ in MDSCs from MC38 and CT26 metastasis tissues, respectively. (K) Liver metastasis from mice was stained for CD11b (green) and Ly6G/Ly6C (red). Inset shows invasion front of liver metastasis. Scale bar = 100 μm, scale bar for zoom out = 30 μm. (L) Quantification of the percent of G-MDSCs in $CD11b^+$, $n = 4$, from MC38 and CT26 metastasis tissues, respectively. (M) Immunohistochemistry staining for CCL9 and CCR1 from MC38 and CT26 metastasis tissues, Scale bar = 100 μm, scale bar for zoom out = 20 μm. (N) Quantification of CCL9 concentration in tumors, $n = 4$. (O) Schematic summary showing SMAD4-deficient CRC recruited $CCR1^+$-G-MDSC *via* the CCL9/CCR1 axis. Data are presented as mean ± SD of at least two independent experiments. Two-tailed unpaired Student's *t*-test (H, L, N), and Brown-Forsythe and Welch ANOVA tests were used (D, F) for statistical analysis with calculated *P* values shown.

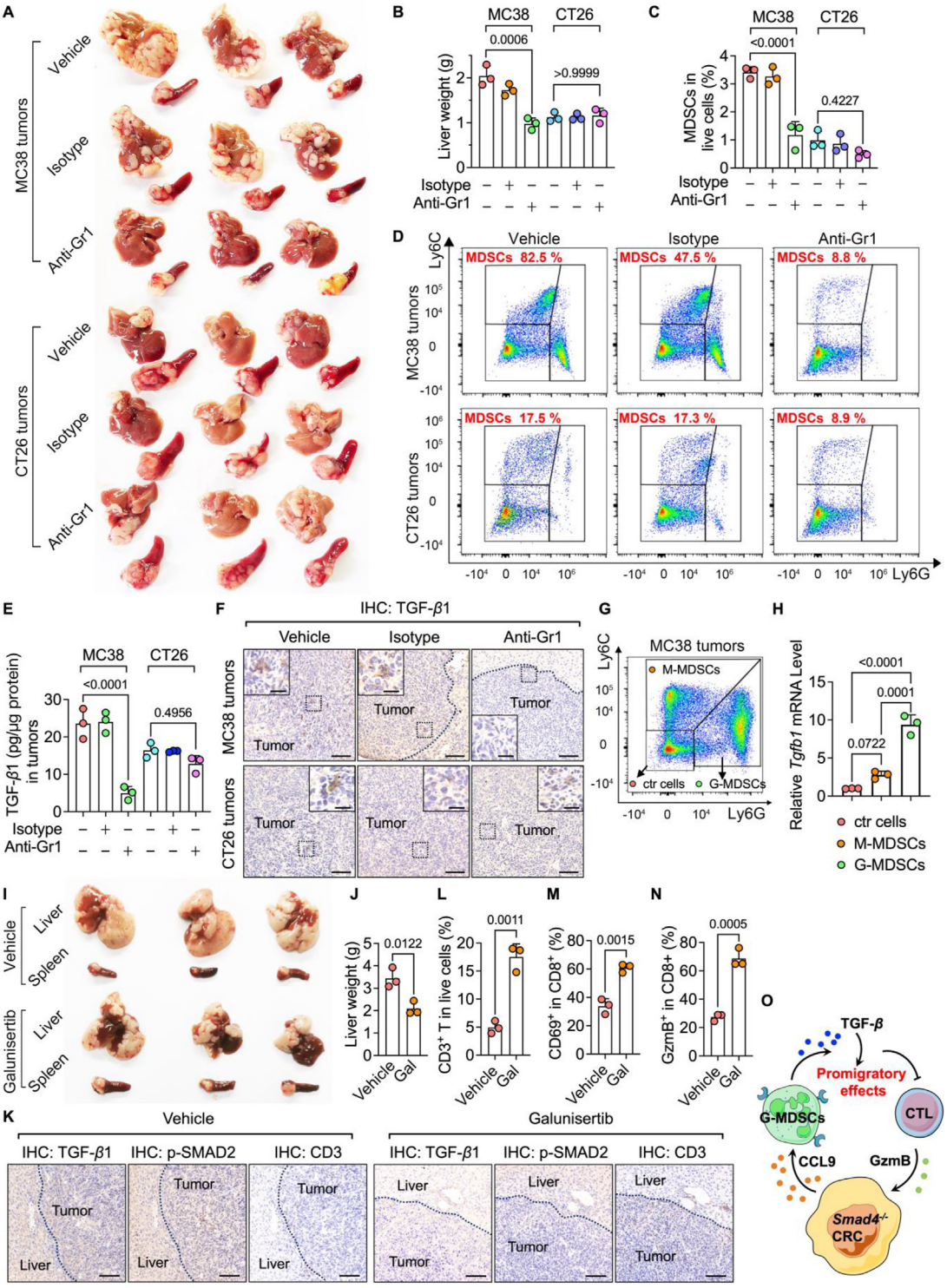

Figure 2 G-MDSCs-derived excessive TGF-β promotes malignant liver metastasis of SMAD4-deficient CRC. (A) MC38 or CT26 cells were injected into spleens of C57BL/6 or BALB/c mice, respectively. Mice received intraperitoneal (i.p.) injection of anti-Gr1 antibody, lgG2b isotype control antibody (200 μg/dose) or vehicle control. Mice were reared for 14 days and sacrificed for analysis of liver metastasis, $n = 3$. (B) Quantification of liver weight, $n = 3$. (C) FACS analysis and quantification of the percent of MDSCs in live cells from MC38 and CT26 metastasis tissues, $n = 3$. (D) Representative FACS plots of MDSCs in $CD11b^{+}$. (E) Quantification of TGF-β1 concentration in tumors from MC38 and CT26 metastasis tissues, $n = 3$. (F) Immunohistochemistry staining for TGF-β1 in metastatic tissues. Scale bar = 100 μm, scale bar for zoom out = 30 μm. (G) Representative FACS plots of sorted G-MDSCs, M-MDSCs and ctr-cells. (H) Relative *Tgfb1* mRNA level in indicated sorted cells, $n = 3$. (I) MC38 cells were injected into the spleens of C57BL/6 mice. Mice received galunisertib (i.g.,75 mg/kg) or vehicle control daily for 7 days. Mice were reared for 7 days and sacrificed for analysis of liver metastasis, $n = 3$. (J) Quantification of liver weight, $n = 3$. Gal: galunisertib. (K) Immunohistochemistry staining for TGF-β1, p-SMAD2 and CD3 of liver metastasis tissues. Scale bar = 100 μm. (L) FACS

Gapdh: (F: 5′-AAGGTCATCCCAGAGCTG-3′ R: 5′-CTGCTTCACCACCTTCTT-3′), *Tgfb1:* (F: 5′-CCCTATATTTGGAGCCTGGA-3′ R: 5′-CTTGCGACCCACGTAGTAGA-3′), *Ccl9:* (F: 5′-TGAAGCCTTTTCATACTGCC-3′ R: 5′-TATTGTTTGTAGGTCCGTGG-3′), *Cxcl13:* (F: 5′-ATAGATCGGATTCAAGTTAC-3′ R: 5′-CTTGGTCCAGATCACAACTT-3′), *Cxr5:* (F: 5′-AAAACGAAGCGGAAACTAG-3′ R: 5′-GGAAGATGACAATGTGGTA-3′), *Il21:* (F: 5′-CAGCATGTGTCAATCACGCTAC-3′ R: 5′-TGTGGTCTTCAGCAGGTTT-3′), *Ifng:* (F: 5′-TGAACGCTACACACTGCATC-3′ R: 5′-CATCCTTTTGCCAGTTCCTC-3′).

2.17. Statistical analysis and reproducibility

The numbers of mice used in each experiment are indicated in figure captions. All data were presented as the mean ± SD. The intergroup comparisons and data statistics were performed with GraphPad Prism 9 software, and statistical significance was calculated as described in figure legends. For all statistical analyses, P value of 0.05 or less was considered statistically significant.

3. Results and discussion

3.1. SMAD4-deficient CRC cells recruit CCR1$^+$-G-MDSCs to tumor tissues

SMAD4 is a tumor suppressor gene located on human chromosome 18q21, which is frequently associated with loss of heterozygosity in CRC progression[36,37]. Previous reports suggested that the loss of SMAD4 facilitated metastasis by accumulating CCR1$^+$-MDSCs in tumor tissues *via* the CCL15/CCR1 axis[3,16,38]. Here, we first analyzed the clinical specimens of primary and metastatic CRC by immunohistochemistry (IHC) and found that 20% of the patients (17 out of 85) were with SMAD4 deficiency, consistent with the frequency previously reported[2]. 70.6% of SMAD4-deficient CRC (12 out of 17) exhibited metastasis (Fig. 1A). Notably, abundant MDSCs expressing the chemokine receptor CCR1 and CD33 were identified in specimens of SMAD4-deficient CRC and CRLM (Fig. 1B), and there was a significant positive correlation between SMAD4 deficiency and the accumulation of CCR1$^+$-cells (Fig. 1C). We then analyzed peripheral blood mononuclear cells (PBMCs) from healthy subjects and patients with primary CRC or metastatic CRC, which were mainly SMAD4 deficient, and found that high levels of MDSC characterized by CD33$^+$, CD11b$^+$, and HLA-DR$^-$ markers were observed in the peripheral blood of patients with metastatic CRC. Moreover, MDSCs from patients with metastatic CRC specifically expressed CCR1, consistent with IHC results of clinical specimens (Fig. 1D and E, Supporting Information Fig. S1A). It was also found that the corresponding chemokine factor CCL15, ectopically expressed by SMAD4-deficient cancer cells, was highly detected in the serum of patients with metastatic CRC (Fig. 1F). Importantly, we found that G-MDSCs, characterized as CD14$^-$, CD15$^+$, CD33$^+$, CD11b$^+$, and HLA-DR$^-$ markers, were the predominant subsets in the metastatic CRC, and the ectopic abundance of G-MDSCs was significantly correlated with the metastatic CRC group (Fig. 1G and H). These findings validated the correlation between SMAD4 deficiency and the accumulation of CCR1$^+$-MDSCs, especially CCR1$^+$-G-MDSCs, *via* the CCL15/CCR1 axis in the metastatic CRC.

To further investigate the correlation, we conducted research using mouse CRC cells. Notably, the MC38 mouse colon cancer cell line, which lacked SMAD4 expression, showed a higher incidence of liver metastasis than CT26 cells, which are typical SMAD4-proficient colon cancer cells, validated by metastatic foci, weight of spleen, and liver (Fig. 1I, Fig. S1B−S1D). Flow cytometry and Western blot analysis validated that CCR1$^+$-MDSCs significantly accumulated in the MC38 metastatic tissues (Fig. 1J, Fig. S1E−S1G). Furthermore, we revealed that G-MDSCs (CD11b$^+$, Ly6G^{high}, Ly6C^{low}) but not the M-MDSCs (CD11b$^+$, Ly6G^{low}, Ly6C^{high}) constituted the predominant cell subset in the MC38 metastatic tumors consistent with human specimens, whereas the CT26 metastatic tumors showed low levels of both G-MDSCs and M-MDSCs (Fig. 1K and L). To investigate whether the intratumoral accumulation of CCR1$^+$-G-MDSCs was related to the CCL9/CCR1 axis, we histologically examined the metastatic tumor tissues in the liver. Consistently, IHC staining and ELISA assays demonstrated that CCR1$^+$ cells accumulated in the invasive front of SMAD4-deficient MC38 tumors along with ectopically abundant CCL9 (the mouse homolog of human CCL15) (Fig. 1M and N). However, there was no significant accumulation of CCR1$^+$ cells or expression of CCL9 in SMAD4-proficient metastatic CT26 cells.

These results indicated that the chemotactic factor CCL9 was ectopically produced by SMAD4-deficient CRC cells, thus explicitly leading to CCR1$^+$-G-MDSC recruitment (Fig. 1O). These findings emphasize the crucial roles played by G-MDSCs in the metastasis of SMAD4-deficient CRC cells.

3.2. CCR1$^+$-G-MDSC-derived excessively TGF-β facilitates metastasis of SMAD4-deficient CRC

Given the high level of CCR1$^+$-G-MDSC accumulated in SMAD4-deficient CRC tumors, we assumed that the infiltration of CCR1$^+$-G-MDSCs facilitated metastasis. To test this hypothesis, we first used an anti-Gr1 antibody to eliminate MDSC *in vivo* (Supporting Information Fig. S2A). Our findings showed that MDSC depletion inhibited the liver metastasis of SMAD4-deficient MC38 cells, as suggested by the metastatic foci, liver weight, and coefficient analysis (Fig. 2A and B, Fig. S2B). However, the depletion of MDSC exerted a negligible effect on the metastasis of SMAD4-proficient CT26 cells. Notably, anti-Gr1 antibody treatment led to a reduced population of both G-MDSC and M-MDSC but did not affect the proportion of G-MDSCs in MDSCs in MC38 metastatic tumors (Fig. 2C and D, Fig. S2C and S2D). It has been reported that G-MDSCs produce TGF-β, and TGF-β suppresses the cytotoxicity program of CD8$^+$ CTLs[39]. We then delved into the effects of MDSC depletion on the levels of TGF-β in both serum and tumor tissues *via* ELISA and IHC staining. Interestingly, MDSC depletion led to a significant

analysis and quantification of the percent of CD3$^+$ T cells in live cells, (M) CD69$^+$ in CD8$^+$ and (N) granzyme B (GzmB$^+$) in CD8$^+$ T cells from liver metastatic tissues, respectively, $n = 3$. (O) Schematic summary of CCR1$^+$-G-MDSC-derived TGF-β promoting malignant liver metastasis of SMAD4-deficient CRC. Data are presented as mean ± SD of at least two independent experiments. Two-tailed unpaired Student's t-test (J, L, M, N) and Ordinary one-way ANOVA with a Tukey's multiple comparisons test (B, C, E, H) were used for statistical analysis with calculated P values shown.

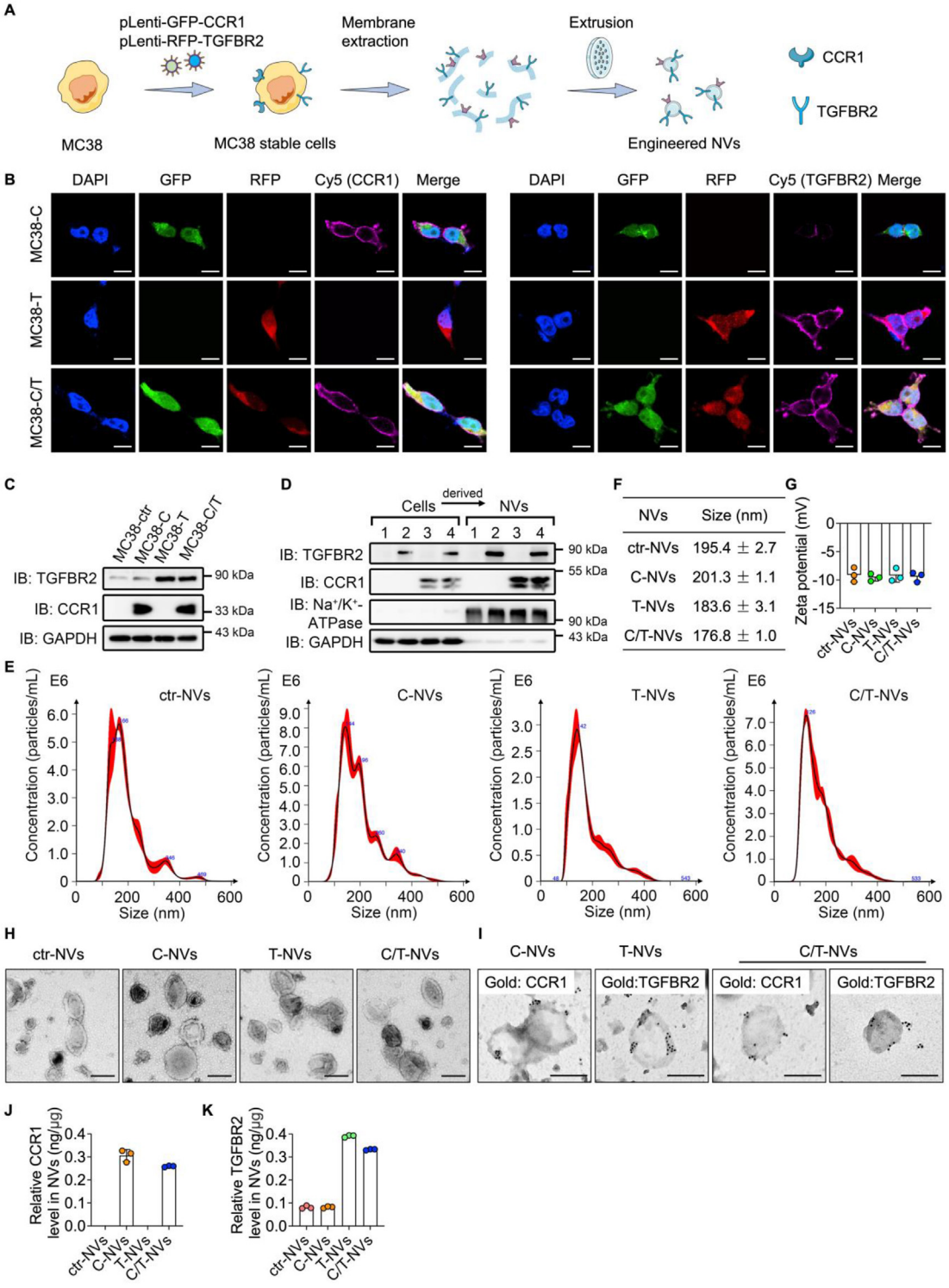

Figure 3 Characterization of CCR1/TGFBR2-engineered NVs. (A) Schematic illustration of the construction of CCR1/TGFBR2-engineered nanovesicles (C/T-NVs). (B) Immunofluorescence staining for CCR1 and TGFBR2 in indicated MC38 stable cell lines. MC38-C: MC38-CCR1 stable cells, MC38-T: MC38-TGFBR2 stable cells, MC38-C/T: MC38-CCR1/TGFBR2 stable cells. Scale bar = 10 μm. (C) Western blot analysis of CCR1 or TGFBR2 in indicated MC38 stable cells. (D) Western blot analysis of stable cells and derived NVs. 1: MC38-ctr and derived ctr-NVs. 2: MC38-T and derived T-NVs. 3: MC38-C and derived C-NVs. 4: MC38-C/T and derived C/T-NVs. (E) Representative nanoparticle tracking analysis (NTA) of size distributions for indicated NVs sample and (F) quantification of corresponding size, $n = 3$. (G) Zeta potential of the engineered NVs, $n = 3$. (H) Representative TEM images of indicated NVs. Scale bar = 200 nm. (I) Representative TEM images of immunogold labeling of CCR1 and TGFBR2 molecules (10 nm nanogold particles) in indicated NVs. Scale bar = 200 nm. (J) The ratio of the CCR1 and (K) TGFBR2 on engineered NVs, $n = 3$. The protein level of CCR1 in ctr-NVs and T-NVs was below the detection limit of the ELISA kit, so it was not shown. Data are presented as mean ± SD.

reduction in the concentration of TGF-β in MC38 metastatic tumors but a partial decrease in serum (Fig. 2E and F, Fig. S2E). These results implied that the intratumoral TGF-β level was related to tumor-infiltrated MDSCs. Here, we observed that depletion of MDSCs did not completely suppress TGF-β expression, suggesting that other essential resources of TGF-β secreted by tumor cells and macrophages are still present to maintain tumor growth[40−42]. To determine which subset of MDSCs is associated with excessive TGF-β secretion, we sorted the tumor-infiltrated G-MDSCs and M-MDSCs by flow cytometry and measured the mRNA level of *Tgfb1* (Fig. 2G). As shown in Fig. 2H—a higher level of TGF-β mRNA was detected in G-MDSCs than in M-MDSCs, suggesting that ectopically excessive TGF-β was primarily derived from infiltrated CCR1$^+$-G-MDSCs in metastatic tumor tissues of SMAD4-deficient CRC. Moreover, MDSC depletion alleviated the TGF-β-inhibited immune response in the MC38 metastasis tissues but not CT26, as evidenced by the increased number of tumoral infiltrated CD3$^+$ T cells (Fig. S2F and S2G), activated CD8$^+$ T cells and granzyme B-positive CTLs (Fig. S2H and S2I) and decreased population of Treg (Fig. S2J).

We next administered galunisertib to evaluate the pathological effects of excessive TGF-β secreted by CCR1$^+$-G-MDSC in the SMAD4-deficient CRC mice model (Fig. S2K). Galunisertib, an efficient inhibitor of TGF-β signaling that directly binds to TGFBR1[43], inhibited the metastasis rate of SMAD4-deficient CRC cells (Fig. 2I and J, Fig. S2L) and profoundly inhibited the proportion of G-MDSCs from 14.9% to 3.93% with a negligible impact on MDSC proficiency in tumors (Fig. S2M and S2N). TGF-β has been reported to play a role in determining the differentiation of G-MDSC subsets[44,45], which may explain the reduction of G-MDSCs affected by galunisertib (Fig. S2M). Galunisertib-induced reduction of G-MDSCs impacted the excessively intratumoral TGF-β but not serum TGF-β (Fig. S2O). Consistently, IHC staining of metastatic tumor tissues demonstrated that galunisertib reduced excessive TGF-β expression and phosphorylation of SMAD2, indicating the blockade of TGF-β signaling (Fig. 2K). In addition, TGF-β signaling inhibition significantly increased the infiltration of CD3$^+$ T cells (Fig. 2L), reduced the proportion of Tregs (Fig. S2P), increased the activation rate of CD8$^+$ T cells, and promoted the proportion of granzyme B-positive CTLs in MC38 metastatic tumors (Fig. 2M and N), consistent with our previously obtained data (Fig. S2G−S2J). These findings suggest that excessive TGF-β, secreted by tumor-infiltrated G-MDSCs, exerts promigratory effects on SMAD4-deficient CRC cells and contributes to Treg infiltration into tumors and CTL inactivation.

Collectively, CCR1$^+$-G-MDSCs contributed to the robust production of excessive TGF-β, which impacted the activation of CTLs, and Treg infiltration, thereby facilitating liver metastasis of SMAD4-deficient CRC cells (Fig. 2O). These findings significantly enhance our understanding of the interplay between the resource of excessive TGF-β and CCR1$^+$-G-MDSCs in the SMAD4-deficient CRC context.

3.3. *Establishment and characterization of CCR1/TGFBR2-engineered NVs*

Given that SMAD4-deficient CRC recruited CCR1$^+$-G-MDSCs to the tumor sites *via* the CCL9/CCR1 axis and CCR1$^+$-G-MDSCs produced excessive TGF-β facilitating malignant metastasis, we engineered nanovesicles (NVs) that displayed dual CCR1 and TGFBR2 molecules, based on the CCL9/CCR1 axis and the association between TGF-β and its specific receptor TGFBR2 (Fig. 3A). NVs could effectively remodel the immunosuppressive tumor microenvironment for enhanced cancer immunotherapy and become an emerging tool as therapeutic agent carriers[46,47]. These nanovesicles would actively target SMAD4-deficient tumors through the CCL9/CCR1 axis, trap intratumorally excessive and essential TGF-β molecules *via* TGF-β-TGFBR2-specific binding, and ultimately inhibit the metastasis of SMAD4-deficient colon cancer. First, we constructed a stable cell line overexpressing CCR1 and TGFBR2 (MC38-C/T) while fluorescence-tagged proteins were expressed simultaneously for labeling. MC38 cells with either expression of CCR1 (MC38-C) or TGFBR2 (MC38-T), as well as wild-type (MC38-ctr), were constructed in subsequent experiments. Immunofluorescence staining results showed that the CCR1 and TGFBR2 proteins were expressed on the cell membranes, consistent with their endogenous localization (Fig. 3B)[48,49]. Additionally, Western blot verified that the MC38-C/T stable cells expressed higher protein levels of CCR1 and TGFBR2 than the MC38-ctr stable cells (Fig. 3C). Western blot result demonstrated that the cell-derived NVs (ctr-NVs from MC38-ctr, C-NVs from MC38-C, T-NVs from MC38-T, and C/T-NVs from MC38-C/T) retained membrane CCR1 and TGFBR2 from parent cells, and a few cytoplasmic components using Na$^+$/K$^+$-ATPase as the intrinsic component of the cell membrane and GAPDH as the intrinsic component of the cell cytoplasm (Fig. 3D). Nanoparticle tracking analysis (NTA) of the NVs indicated that the four engineered NVs had an average diameter of $\sim$200 nm, a Zeta potential of $\sim$ −10 mV, and a negligible difference among them (Fig. 3E−G, Supporting Information Fig. S3A). No significant size changes and protein expression ratio of NVs in PBS were observed after 7 days, which fulfilled the specific requirements for intravenous (i.v.) injection (Fig. S3B and S3C). Transmission electron microscopy (TEM) revealed that the four engineered NVs displayed the characteristic cup-shaped morphology and displayed similar diameters of $\sim$200 nm (Fig. 3H), consistent with the NTA results (Fig. 3E). Additionally, immunogold electron microscopy provided further evidence of the presence of CCR1 and TGFBR2 on the membranes of the NVs (Fig. 3I, Fig. S3D). 0.2591 $\pm$ 0.0029 ng of CCR1 and 0.3325 $\pm$ 0.0027 ng of TGFBR2 molecules were present per 1 μg of the engineered vesicles. There was undetectable expression of CCR1 and 0.0814 $\pm$ 0.0066 ng/μg protein on the control vesicles (Fig. 3J and K). These findings definitively confirmed the successful engineering of NVs.

3.4. *C/T-NVs chemotactically target SMAD4-deficient CRC cells and trap intratumoral TGF-β*

Modifying the NVs with CCR1 was expected to target SMAD4-deficient CRC tumors *via* the CCL9/CCR1 axis chemotactically. To test this hypothesis, we established an *in vitro* chemotactic response model using Transwell chambers. First, we validated that CCR1-engineered (CCR1$^+$) cells showed chemotactic responses to CCL9. We seeded CCR1$^+$ or CCR1$^-$ cells in the upper compartment of the chamber and added the indicated culture medium with or without CCL9 to the lower compartment of the chamber with a slide. The transferred cells on the slide were stained with crystal violet (Fig. 4A). Interestingly, CCR1$^+$ cells but not CCR1$^-$ cells migrated to the lower compartment, indicating a significant chemotactic response to CCL9. Furthermore, CCR1$^+$ cells showed a similar response to MC38-culture

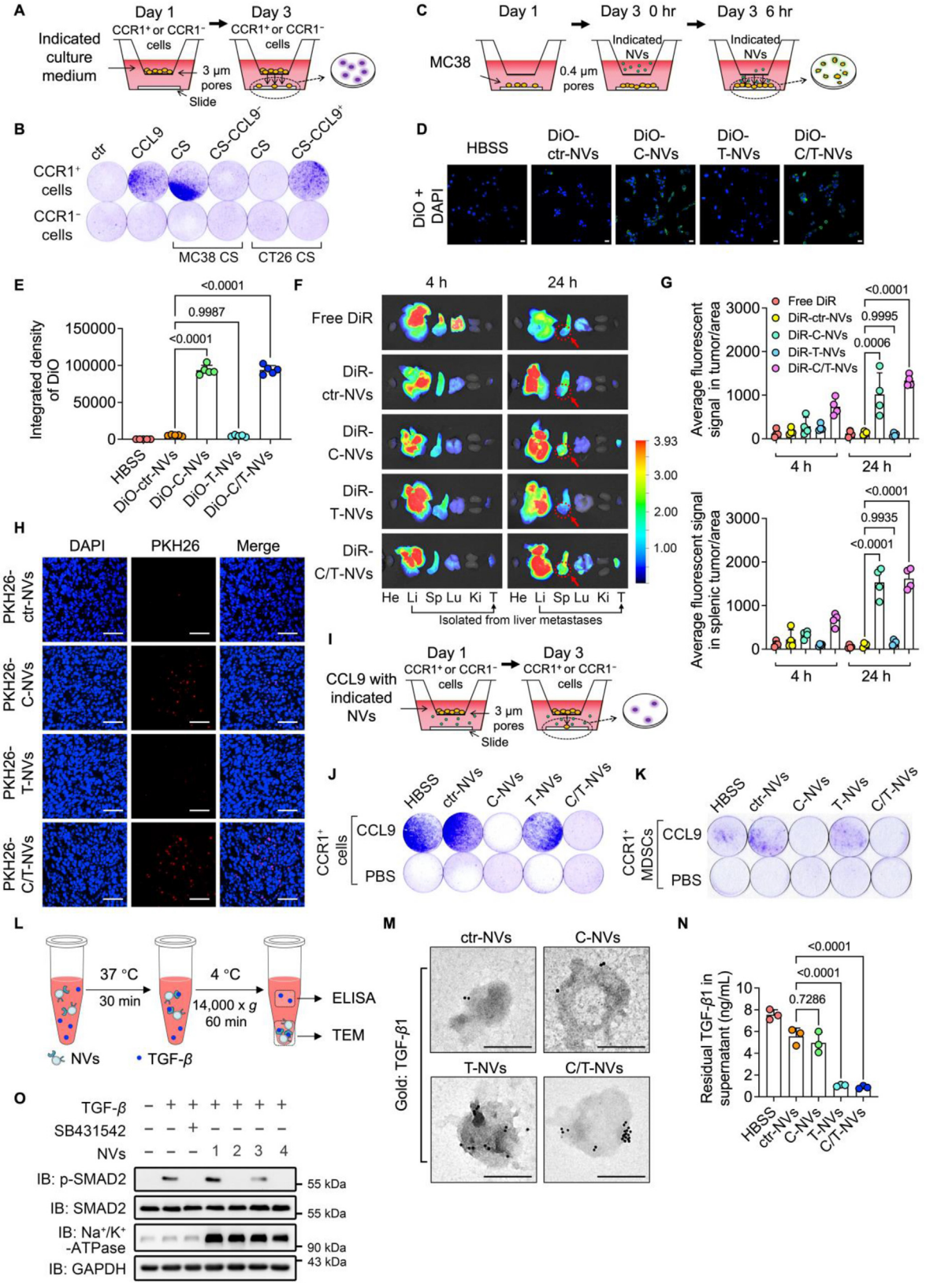

Figure 4 C/T-NVs chemotactically target SMAD4-deficient tumor cells and trap TGF-β molecules. (A) Transwell to investigate chemotactic migration of CCR1$^+$ cells to CCL9. (B) Migratory cells on the slide were stained and photographed. CS, cultured supernatant. (C) Transwell to investigate the chemotaxis of CCR1$^+$ NVs to SMAD4-deficient cells. (D) DiO-NVs (green) and MC38 cells were stained with DAPI (blue) for CLSM image, Scale bar = 10 μm. (E) Quantification of the integrated density of DiO in each image analyzed by Image J, $n = 5$. (F) The *ex vivo* biodistribution of free DiR and indicated DiR-NVs in spontaneous metastasis model at 4 and 24 h post intravenous injection. He: heart, Li: liver,

supernatant (as indicated by MC38-CS) and negligible chemotaxis to MC38-CS-CCL9^{-} (CCL9 depletion using a specific antibody). In contrast, CT26-culture supernatant (CT26-CS) exerted negligible recruitment effect on CCR1^{+} cells, while CCL9 supplement (CT26-CS-CCL9^{+}) reversed the outcome (Fig. 4B). These results demonstrated that CCR1^{+} cells showed a chemotactic response with CCL9 *via* the CCL9-CCR1 axis. To further explore the chemotaxis of CCR1-engineered NVs, we seeded MC38 cells that sustainably secreted CCL9 in the lower compartment of the chamber and added DiO-labeled NVs to the upper compartment (Fig. 4C). CCR1^{+} NVs (C-NVs and C/T-NVs), but not CCR1^{-} NVs (ctr-NVs and T-NVs), exhibited a chemotactic response to MC38 cells (Fig. 4D and E). These results suggested that CCR1^{+} NVs actively targeted MC38, the SMAD4-deficient cancer cell line, in a chemokine-responsive manner *in vitro*. We further explored the chemotaxis of the engineered NVs *ex vivo*. As anticipated, DiR-labeled CCR1^{+} NVs were significantly distributed to liver metastasis and primary splenic tumors indicated by the near-infrared fluorescence imaging system and quantitative analysis after 24-h distribution (Fig. 4F and G, Supporting Information Fig. S4A). Furthermore, PKH26-labeled CCR1^{+} NVs were accumulated in tumor tissues, while CCR1^{-} NVs did not achieve intratumoral aggregation (Fig. 4H, Fig. S4B). To investigate the underlying mechanism, we analyzed the CCL9 concentration in separate sections of tumors. The results showed that tumor tissues exhibited a higher CCL9 mRNA level than paracancerous tissue in liver metastatic and primary splenic tumors (Fig. S4C). The concentration gradient of CCL9 implied a chemotactic response by CCR1-engineered nanovesicles. We then conducted a thorough investigation into the potential competitive relationship between CCR1^{+}-G-MDSCs and CCR1^{+}-NVs, as the CCL9-CCR1 axis is critical for the active recruitment of both the cells and NVs to tumor tissues. To simulate the recruitment of NVs to the microenvironment through this axis, we added NVs and CCL9 directly to the lower compartment (Fig. 4I). Our findings revealed that CCR1^{+} NVs significantly hindered the migration of CCR1^{+} cells but not CCR1^{-} cells, whereas CCR1^{-} NVs in the lower chamber exerted a minimal impact (Fig. 4J, Fig. S4D). Additionally, we observed that the chemotactic response of sorted intratumoral CCR1^{+}-G-MDSCs was inhibited by CCR1^{+} NVs *via* blockade of the CCL9-CCR1 axis (Fig. 4K, Fig. S4E). These results indicate that SMAD4-deficient CRC cells actively recruited CCR1^{+}-NVs, which chemotactically accumulated, *via* the CCR1-CCL9 axis, ultimately counteracting the accumulation of CCR1^{+} cells, particularly CCR1^{+}-G-MDSCs, through direct binding and depletion of CCL9 in the tumor microenvironment.

Given the chemotactic tumor targeting of CCR1^{+} NVs, we conducted an assay to investigate the function of TGFBR2-engineered NVs (TGFBR2^{+} NVs) (Fig. 4L). Immunogold electron microscopy and ELISA results demonstrated that the TGFBR2^{+} NVs (T-NVs and C/T-NVs) trapped and eliminated TGF-β molecules (Fig. 4M and N). TGF-β initiates signal transduction by binding to TGFBR2, which leads to the phosphorylation of SMAD2[50]. To explore whether TGFBR2^{+} NVs blocked TGFβ signaling, we performed a Western blot analysis to detect the phosphorylation rate of SMAD2. As expected, TGF-β induced the phosphorylation of SMAD2, which was potently inhibited by the TGFBR-specific inhibitor SB431542. Notably, TGFBR2^{+} NVs inhibited the TGF-β-induced phosphorylation of SMAD2 in a dose-dependent manner (Fig. S4F), and 5E09 count of TGFBR2^{+} NVs exerted a significant inhibitory effect similar to that of SB431542 (Fig. 4O).

Collectively, these findings indicated that NVs engineered with dual CCR1 and TGFBR2 molecules chemotactically targeted SMAD4-deficient tumor tissues and attenuated the accumulation of CCR1^{+}-G-MDSCs *via* the CCL9/CCR1 axis. Additionally, engineered NVs trapped TGF-β molecules through specific binding of TGF-β-TGFBR2 to reduce TGF-β, leading to the inhibition of TGF-β signaling.

3.5. *C/T-NVs attenuate liver metastasis of SMAD4-deficient CRC and facilitate infiltration of CTLs*

To further explore the therapeutic capabilities of C/T-NVs for metastasis of SMAD4-deficient CRC, a spontaneous metastasis model using luciferase-expressing MC38 cells (MC38-Luc) was constructed with NVs administration, allowing monitoring of metastasized tumor cells in the liver *via* bioluminescence (Supporting Information Fig. S5A). Notably, bioluminescence intensity increased significantly on Day 4 after the splenic injection of MC38-luc cells. By Day 7, MC38-luc exhibited liver metastasis, and the metastasis rate was continuously increased over the following 6 days. C-NVs and T-NVs interventions partially inhibited liver metastasis, while C/T-NVs potently attenuated the metastasis (Fig. 5A and B). To comprehensively explore the mechanisms underlying these outcomes, we established the MC38 spontaneous metastasis model and examined immune responses to NV intervention. Consistent with the therapeutic effect in the MC38-luc model (Fig. S5B), C/T-NVs exhibited a more significant antimetastatic effect than C-NVs, T-NVs, or ctr-NVs, validated by liver weight and coefficient results (Fig. 5C and D, Fig. S5C). However, C/T-NVs intervention showed a negligible change in body weight compared to galunisertib, which induces systemic blockade of TGF-β, indicating that NV-based receptor-ligand traps efficaciously deplete intratumoral TGF-β but not systemic TGF-β with a low systemic side effect (Fig. S5C, Fig. S2L). Notably, mice treated with C/T-NVs showed significantly prolonged survival, living for over 60 days compared to those treated with vehicle, ctr-NVs, and C-NVs (dying within 40 days) or T-NVs (living for over 50 days) (Fig. 5E). CCR1^{+} NVs significantly reduced the concentration of CCL9 in tumors and plasma, the population of tumor-infiltrated MDSCs, and the

Sp: spleen, Lu: lung, Ki: kidney, T: tumor. (G) Quantification of average DiR fluorescent signal in isolated liver metastasis sections and splenic tumors, $n = 4$. (H) Immunofluorescence image of PKH26-NVs biodistribution in tumor tissue at 24 h post intravenous injection. Scale bar = 100 μm. (I) Transwell to investigate the counteracting effect of CCR1^{+} NVs on the chemotactic migration of CCR1^{+} cells. (J) Migratory CCR1^{+} cells and (K) sorted intratumoral CCR1^{+} MDSCs, respectively were stained and photographed. (L) Schematic diagram of TGFBR2^{+} NVs trapping TGF-β1 molecules. (M) Representative TEM images of trapped TGF-β1 molecular (10 nm immunogold labeling) on indicated NVs. Scale bar = 200 nm. (N) Quantification of residual TGF-β1 in supernatant, $n = 3$. (O) Western blot analysis of MC38 cells treated with SB431542 or 5E09 count NVs. 1: ctr-NVs. 2: T-NVs. 3: C-NVs. 4: C/T-NVs. Data are presented as mean ± SD of at least two independent experiments. Ordinary one-way ANOVA with a Tukey's multiple comparisons test (E, G, N) was used for statistical analysis with calculated *P* values shown.

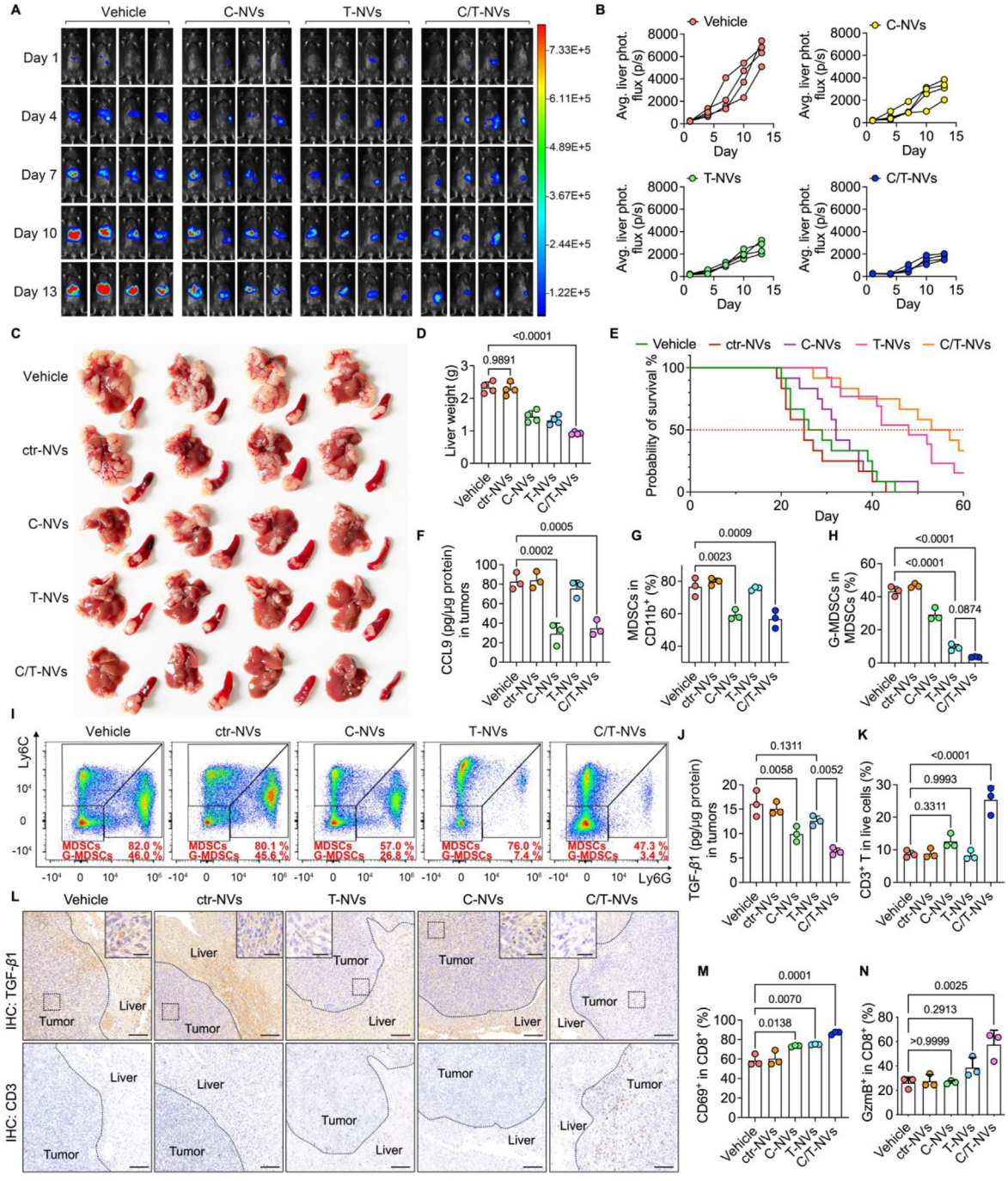

Figure 5 C/T-NVs attenuate liver metastasis of SMAD4-deficient CRC. (A) MC38-Luc cells were injected into the spleens of C57BL/6 mice. Mice received 5E11 count of indicated NVs and HBSS vehicle (i.v.), respectively. *In vivo* bioluminescence images of MC38-Luc metastases in indicated groups at indicated time point and (B) quantification of liver photon flux of each mouse, $n = 4$. (C) MC38 cells were injected into the spleens of C57BL/6 mice. Mice received 5E11 count of indicated NVs and HBSS vehicle (i.v.), respectively. Mice were reared for 14 days and sacrificed for analysis of liver metastasis, $n = 4$. (D) Quantification of the liver weight, $n = 4$. (E) Overall survival time of mice in indicated groups, $n = 12$. (F) Quantification of CCL9 concentration in tumors with indicated NVs treatment, $n = 3$. (G) FACS analysis and quantification of the percent of MDSCs in $CD11b^+$, (H) G-MDSCs in MDSCs in metastatic tumors, respectively, $n = 3$. (I) Representative FACS plots of G and H. (J) Quantification of TGF-β1 concentration in tumors with indicated NVs treatment, $n = 3$. (K) FACS analysis and quantification of the percent of $CD3^+$ in live cells in liver metastasis, $n = 3$. (L) Immunohistochemistry staining for TGF-β1 and CD3 of liver metastasis. Inset shows invasion front of liver metastasis. Scale bar = 100 μm, scale bar for zoom out = 30 μm. (M) FACS analysis and quantification of the percent of $CD69^+$ and (N) granzyme B ($GzmB^+$) in $CD8^+$ cells in liver metastasis, respectively, $n = 3$. Data are presented as mean ± SD of at least two independent experiments. Ordinary one-way ANOVA with a Tukey's multiple comparisons test (D, F, G, H, J, K, M, N) was used for statistical analysis with calculated *P* values shown.

proportion of G-MDSCs (Fig. 5F−I, Fig. S5D). Moreover, C/T-NVs showed a more significant inhibitory effect than C-NVs on G-MDSC infiltration, suggesting the crucial role displayed by the TGFBR2 region. In addition, C/T-NVs and T-NVs were equally effective in reducing TGF-β levels in plasma (Fig. S5E). However, the C/T-NVs showed greater efficiency in counteracting intratumoral TGF-β, suggesting the crucial role displayed by the CCR1 region, which chemotactically drove NVs to tumors (Fig. 5J and L). We found that C-NVs alone could inhibit the excessive TGF-β by inhibiting the accumulation of G-MDSCs in the tumor. Nevertheless, C/T-NVs could further reduce the concentration of intratumoral TGF-β (Fig. 5J and L), suggesting that the modifying TGFBR2 regions could exhaust the essential TGF-β. The exhaustion of both excessive and essential TGF-β effectively increased the tumor-infiltrated $CD3^+$ T lymphocytes (Fig. 5K and L), the population of activated $CD8^+$ T cells indicated by $CD69^+$ and the infiltration of granzyme B-positive CTLs (Fig. 5M and N). In addition, C/T-NVs reduced the proportion of Tregs, a subset of lymphocytes regulated by TGF-β (Fig. S5F−S5H). These results demonstrated that the C/T-NVs effectively induced an antimetastatic immune response by counteracting both excessive and essential TGF-β in SMAD4-deficient CRC.

3.6. C/T-NVs combined with aPD-L1 facilitate the formation of TLSs around tumors and eradicate metastatic foci

SMAD4 negatively regulates the expression of the epithelial immune checkpoint molecule PD-L1 in human gastric cancer (GC) cells[8]. To investigate the effect of SMAD4 deficiency on PD-L1 in CRC cells, we reanalyzed clinical specimens of human CRC. Here, IHC staining revealed that the expression of PD-L1 in SMAD4-deficient CRC was higher than that in SMAD4-proficient CRC, indicating a significant positive correlation between SMAD4-deficiency and PD-L1 expression (Fig. 6A and B). We also validated the high concentration of TGF-β in SMAD4-deficient CRC (Fig. 6A). High levels of TGF-β and PD-L1 resulted in the maintenance of an immunosuppressive microenvironment. Reactivating tumor-infiltrating T cells with immune checkpoint blockade therapies such as aPD-L1 contributed to long-term survival for patients. As a promising therapy, aPD-L1 impairs the PD-1/PD-L1 axis and reactivates the antitumor immune response. Nevertheless, TGF-β hampers the therapeutic effect of aPD-L1 by impeding the expansion of stem-like $CD8^+$ T cells[51]. Therefore, we hypothesized that combining engineered NV-induced TGF-β inhibition with aPD-L1 may be curative immunotherapy (Supporting Information Fig. S6A). Indeed, the combination of aPD-L1 and ctr-NVs effectively inhibited liver metastasis of MC38 cells and tumor growth in the spleen compared to the effects of the vehicle and ctr-NVs. C/T-NVs showed notable inhibition of metastasis but exerted a negligible effect on splenic tumor growth. The C/T-NVs and aPD-L1 combination demonstrated significant antitumor activity, inhibiting liver metastasis and reducing the size of splenic tumors *in situ* (Fig. 6C and D, Fig. S6B). These findings indicate that simultaneously inhibiting PD-L1 and the immunosuppressive cytokine TGF-β effectively reduces the metastasis of SMAD4-deficient CRC cells and suppresses tumor growth. We conducted further analysis of the synergistic combination and found that C/T-NVs exerted a significant inhibitory effect on the concentration of intratumoral TGF-β, the population of MDSC, and the infiltration of G-MDSCs, consistent with the previously obtained results. However, the combination with aPD-L1 led to negligible changes (Fig. 6E and F, Fig. S6C and S6D), indicating that the synergistic effect did not rely on TGF-β concentration and the infiltration of myeloid cells. In addition to myeloid cells, we investigated the effects on lymphocyte infiltration. The combination of aPD-L1 and C/T-NVs significantly increased the amount of tumoral infiltration of $CD45^+$ immune cells and $CD3^+$ T cells (Fig. 6G, Fig. S6E). Notably, this combination also effectively increased the amount of tumor-infiltrated and activated $CD8^+$ T cells and promoted the proportion of granzyme B-positive CTLs (Fig. 6H, Fig. S6F and S6G). Additionally, the combination effectively increased the amount of tumor-infiltrated activated $CD4^+$ T cells indicated by $CD69^+$, and activated $B220^+$ B cells indicated by $CD69^+$ and MHC-II^+ $CD80^+$ (Fig. 6I and J, Fig. S6H). IHC staining demonstrated that the combination therapy increased the intratumoral infiltration rates of $CD20^+$ B cells and $CD3^+$ T cells, along with a significant reduction of TGF-β molecules and markedly increased the necrotic area of metastatic tumors, as marked by the red dotted line (Fig. 6K, Fig. S6I). Interestingly, the simultaneous inhibition of PD-L1 and TGF-β signaling led to significant aggregation and infiltration of $CD20^+$ B-cell clusters surrounded with $CD3^+$ T cells around tumor tissues. In contrast, negligible clustered lymphocytes were observed in the vehicle, ctr-NVs, ctr-NVs + aPD-L1, and C/T-NVs groups (Fig. 6K). The appearance of lymphocyte clusters suggested the formation of tertiary lymphoid structures (TLSs) in the tumor.

The presence of TLSs at metastatic foci is crucial for the level of tumor-infiltrated lymphocytes, which directly determine the antitumor effects[52,53]. TLSs potentially activate effector T cells within tumors, serving as immune cell factories that can lead to robust antitumor effects and eradicate the tumor, providing a new perspective for potentially curative treatment of SMAD4-deficient CRC. TLS formation is indicated by two molecules, CXCL13 and CXCR5, which are expressed predominantly in $CD4^+$ T cells and $CD20^+$ B cells, respectively[54,55]. Consistently, the combination of C/T-NVs and aPD-L1 markedly increased the gene expression of *Cxcl13* and *Cxcr5* (Fig. 6L and M). IHC and immunofluorescence staining validated that CXCR5-positive $CD20^+$ B cells formed clusters surrounded by CXCL13-positive $CD4^+$ T cells and scattered $CD8^+$ CTLs. Additionally, high endothelial venules (HEV), specialized blood vessel structures involved in the recruitment of lymphocytes, were observed in the clustered structure (Fig. S6J). Ki67-positive staining demonstrated that the clustered lymphocytes associated with HEV showed the ability to proliferate (Fig. 6N). The molecular markers IL21 and IFN-γ, which maintained the cytotoxic effect of TLSs, were highly expressed (Fig. 6N−P). All these molecular properties, which are necessary for TLS formation, indicated that the combination of C/T-NVs and aPD-L1 facilitated TLS formation. The formation of TLSs indicated the synergistic antitumor effects mediated by the combination of C/T-NVs and aPD-L1. Numerous trials based on the dual inhibition of TGF-β signaling and PD-L1 reduction effectively inhibit tumors without forming TLSs[56−58]. However, the combination of aPD-L1 and C/T-NV-induced blockade of TGF-β signaling leads to the formation of these structures. The critical factor for TLS formation is the sufficient antigens to be recognized by antigen-presenting cells (APCs)[52,55]. It has been reported that tumor cell-derived NVs contain a large spectrum of tumor-specific antigens that can elicit antitumor immunity by promoting the proliferation of $CD4^+$ T cells and APCs maturation[59-61]. Further, MDSCs repel TLS-derived T and B cells in physical proximity through cell−cell interactions[62]. APCs maturation induced by tumor-derived NVs, C/T-NV-mediated inhibition of

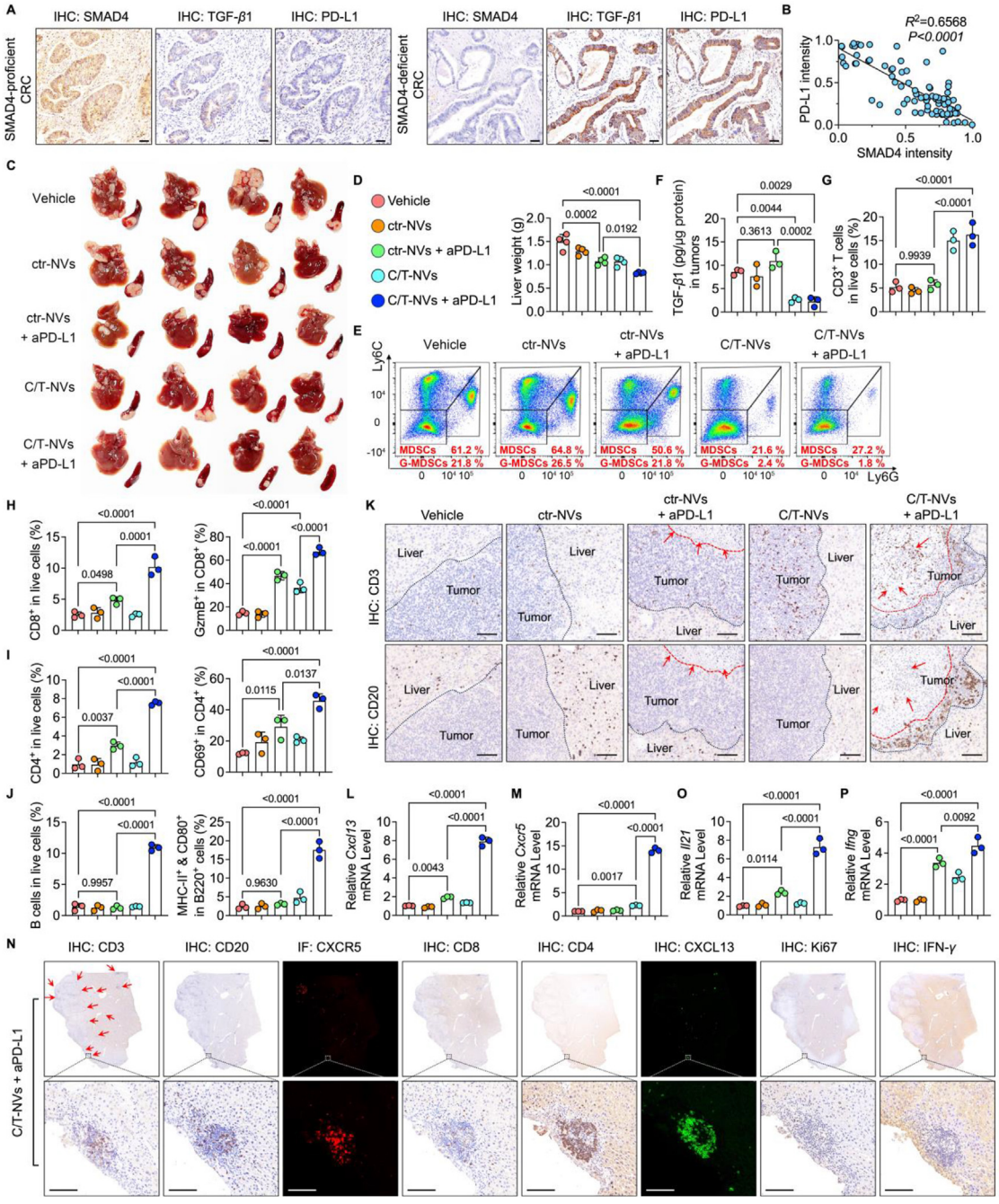

Figure 6 The combination of C/T-NVs and aPD-L1 facilitates the formation of tertiary lymphoid structures around tumors and eradicates metastatic foci. (A) Immunohistochemistry staining for SMAD4, TGF-β1 and PD-L1 of clinical specimens of human primary CRC with SMAD4 deficiency or proficiency. Scale bar = 100 μm. (B) Pearson correlation between the SMAD4 intensity and PD-L1 intensity in immunohistochemistry image of human CRC. (C) MC38 cells were injected into the spleens of C57BL/6 mice. Mice were treated with HBSS vehicle, ctr-NVs, ctr-NVs + aPD-L1, C/T-NVs, and C/T-NVs + aPD-L1. Mice were reared for 14 days and sacrificed for analysis of liver metastasis, $n = 4$. (D) Illustration of indicated groups for the following figures and quantification of liver weight, $n = 4$. (E) Representative FACS plots of the percent of MDSCs and G-MDSCs in liver metastasis. (F) Quantification of TGF-β1 concentration in tumors with indicated treatment, $n = 3$. (G) FACS analysis and quantification of the percent of $CD3^+$ in live cells, (H) $CD8^+$ in live cells, granzyme B ($GzmB^+$) in $CD8^+$, (I) $CD4^+$ in live cells, $CD69^+$ in $CD4^+$, (J) $B220^+$ B in live cells and $MHC\text{-}II^+$, $CD80^+$ in $B220^+$, respectively, $n = 3$. (K) Immunohistochemistry staining for CD3 and CD20 of liver metastasis. Black insets show invasion front of liver metastasis. Red insets and arrows show the necrosis area. Scale bar = 100 μm. (L) Relative mRNA level of *Cxcl13*, (M) *Cxcr5* in liver metastasis with indicated treatment, respectively, $n = 3$. (N) Representative images of immunohistochemistry staining for CD3, CD20, CD8, CD4, Ki67, IFN-γ and immunofluorescence staining for CXCR5, CXCL13 for analysis of the formation of TLS. Red arrows show TLSs. Scale bar = 100 μm. (O) Relative mRNA level of *Il21*, (P) *Ifng* in liver metastasis with indicated treatment, respectively, $n = 3$. Data are presented as mean ± SD of at least two independent experiments. Ordinary one-way ANOVA with a Tukey's multiple comparisons test (D, F, G, H, I, J, I, M, O, P) was used for statistical analysis with calculated *P* values shown.

TGF-β signaling, and C/T-NV-mediated accumulation of MDSCs might play an essential role in the formation of TLSs.

4. Conclusions

Although SMAD4 deficiency is strongly implicated in the metastasis of CRC, the underlying mechanisms remain to be fully elucidated. The study provides details on immune cell infiltration-medicated metastasis. (1) SMAD4-deficient tumor cells abnormally express chemokine CCL9 and PD-L1. (2) $CCR1^+$-G-MDSCs accumulate at tumor sites *via* the CCL9/CCR1 axis. (3) $CCR1^+$-G-MDSCs produce abundant TGF-β. (4) TGF-β along with synergistically expressed PD-L1, directly inhibits the activity of CTLs and promotes metastasis. Based on the metastatic mechanism of SMAD4-deficient CRC, we constructed immunotherapeutic nanovesicles named C/T-NVs, which were engineered with two functional regions: CCR1 as an active targeting region and a TGFBR2 region for TGF-β capture. C/T-NVs actively target tumors *via* the CCL9/CCR1 axis and hinder the association between the $CCR1^+$-G-MDSCs and the CCL9/CCR1 axis, thus decreasing excessive TGF-β. Furthermore, tumor-infiltrated C/T-NVs trap essential TGF-β leading to TGF-β signaling blockade completely, which results in the Tregs reduction and tumor-infiltrated CTL activation. The overall outcomes induced by C/T-NVs demonstrate a decelerated metastasis of SMAD4-deficient CRC. Nevertheless, the combined treatment of C/T-NVs and aPD-L1, which simultaneously target the synergistic promigratory factors, leads to the formation of mature TLSs with a potent immune response by tumor-infiltrated CTLs and eradicates metastases. In conclusion, this study emphasizes that $CCR1^+$-G-MDSC subsets dominate the promigratory effects by producing abundant TGF-β in the metastatic progression, providing a mechanical basis for MDSC infiltration-related metastasis of SMAD4-deficient CRC. And demonstrates that C/T-NVs impede the metastasis of SMAD4-deficient CRC cells *via* pleiotropic effects on the immune response of $CD4^+$ T, $CD8^+$ T, $CD20^+$ B cells, and TLS formation, inspiring the therapy of SMAD4-deficient cancers in clinical practice.

Acknowledgments

This work was supported by National Natural Science Foundation of China (Nos. 82204309, 82103459), China Postdoctoral Science Foundation (No. 2021M701327) and the Program for HUST Academic Frontier Youth Team (No. 2018QYTD13, China). Thanks to the scanning electron microscopy analysis provided by the Analytical and Testing Center of Huazhong University of Science and Technology, and animal care provided by Laboratory Animal Center of Huazhong University of Science and Technology.

Author contributions

Boning Niu: Conceptualization, Data curation, Funding acquisition, Investigation, Methodology, Project administration, Resources, Validation, Writing − original draft, Writing − review & editing. Tianyi Tian: Data curation, Formal analysis, Investigation, Writing − original draft, Writing − review & editing. Lu Wang: Data curation, Formal analysis, Funding acquisition, Methodology, Validation, Writing − original draft. Yinmei Tian: Methodology, Validation, Investigation. Tian Tian: Formal analysis, Investigation, Validation. Yuanyuan Guo: Formal analysis, Investigation, Writing − original draft. Hu Zhou: Methodology, Writing − review & editing. Zhiping Zhang: Funding acquisition, Resources, Supervision, Writing − original draft, Writing − review & editing, Conceptualization.

Conflict of interest

The authors have no conflicts of interest to declare.

Appendix A. Supporting information

Supporting information to this article can be found online at https://doi.org/10.1016/j.apsb.2024.05.009.

References

1. Kuipers EJ, Grady WM, Lieberman D, Seufferlein T, Sung JJ, Boelens PG, et al. Colorectal cancer. *Nat Rev Dis Prim* 2015;**1**:15066.
2. Papageorgis P, Cheng K, Ozturk S, Gong Y, Lambert AW, Abdolmaleky HM, et al. Smad4 inactivation promotes malignancy and drug resistance of colon cancer. *Cancer Res* 2011;**71**:998−1008.
3. Inamoto S, Itatani Y, Yamamoto T, Minamiguchi S, Hirai H, Iwamoto M, et al. Loss of SMAD4 promotes colorectal cancer progression by accumulation of myeloid-derived suppressor cells through the CCL15−CCR1 chemokine axis. *Clin Cancer Res* 2016;**22**:492−501.
4. Alazzouzi H, Alhopuro P, Salovaara R, Sammalkorpi H, Jarvinen H, Mecklin JP, et al. SMAD4 as a prognostic marker in colorectal cancer. *Clin Cancer Res* 2005;**11**:2606−11.
5. Massagué J, Seoane J, Wotton D. Smad transcription factors. *Gene Dev* 2005;**19**:2783−810.
6. Yang G, Yang X. Smad4-mediated TGF-β signaling in tumorigenesis. *Int J Biol Sci* 2010;**6**:1−8.
7. Shi YG, Massagué J. Mechanisms of TGF-β signaling from cell membrane to the nucleus. *Cell* 2003;**113**:685−700.
8. An HW, Seok SH, Kwon JW, Choudhury AD, Oh JS, Voon DC, et al. The loss of epithelial Smad4 drives immune evasion *via* CXCL1 while displaying vulnerability to combinatorial immunotherapy in gastric cancer. *Cell Rep* 2022;**41**:111878.
9. Wasserman I, Lee LH, Ogino S, Marco MR, Wu C, Chen X, et al. SMAD4 loss in colorectal cancer patients correlates with recurrence, loss of Immune Infiltrate, and chemoresistance. *Clin Cancer Res* 2019;**25**:1948−56.
10. Zhang B, Zhang B, Chen X, Bae S, Singh K, Washington MK, et al. Loss of Smad4 in colorectal cancer induces resistance to 5-fluorouracil through activating Akt pathway. *Br J Cancer* 2014;**110**:946−57.
11. Niu B, Liu J, Lv B, Lin J, Li X, Wu C, et al. Interplay between transforming growth factor-beta and Nur77 in dual regulations of inhibitor of differentiation 1 for colonic tumorigenesis. *Nat Commun* 2021;**12**:17.
12. O'Brien CA, Kreso A, Ryan P, Hermans KG, Gibson L, Wang Y, et al. ID1 and ID3 regulate the self-renewal capacity of human colon cancer-initiating cells through p21. *Cancer Cell* 2012;**21**:777−92.
13. Cortez VS, Ulland TK, Cervantes-Barragan L, Bando JK, Robinette ML, Wang Q, et al. SMAD4 impedes the conversion of NK cells into ILC1-like cells by curtailing non-canonical TGF-β signaling. *Nat Immunol* 2017;**18**:995−1003.
14. Frey P, Devisme A, Rose K, Schrempp M, Freihen V, Andrieux G, et al. SMAD4 mutations do not preclude epithelial-mesenchymal transition in colorectal cancer. *Oncogene* 2022;**41**:824−37.

15. Trikha P, Carson WE. Signaling pathways involved in MDSC regulation. *Biochim Biophys Acta Rev Cancer* 2014;**1846**:55−65.
16. Itatani Y, Kawada K, Fujishita T, Kakizaki F, Hirai H, Matsumoto T, et al. Loss of SMAD4 from colorectal cancer cells promotes CCL15 expression to recruit CCR1+ myeloid cells and facilitate liver metastasis. *Gastroenterology* 2013;**145**:1064−75.
17. Li B, Zhang S, Huang N, Chen H, Wang P, Yang J, et al. CCL9/CCR1 induces myeloid-derived suppressor cell recruitment to the spleen in a murine H22 orthotopic hepatoma model. *Oncol Rep* 2018;**41**:608−18.
18. Kitamura T, Kometani K, Hashida H, Matsunaga A, Miyoshi H, Hosogi H, et al. SMAD4-deficient intestinal tumors recruit CCR1+ myeloid cells that promote invasion. *Nat Genet* 2007;**39**:467−75.
19. Li F, Du X, Lan F, Li N, Zhang C, Zhu C, et al. Eosinophilic inflammation promotes CCL6-dependent metastatic tumor growth. *Sci Adv* 2021;**7**:eabb5943.
20. Zhang C, Yi W, Li F, Du X, Wang H, Wu P, et al. Eosinophil-derived CCL-6 impairs hematopoietic stem cell homeostasis. *Cell Res* 2018;**28**:323−35.
21. Ouzounova M, Lee E, Piranlioglu R, El Andaloussi A, Kolhe R, Demirci MF, et al. Monocytic and granulocytic myeloid derived suppressor cells differentially regulate spatiotemporal tumour plasticity during metastatic cascade. *Nat Commun* 2017;**8**:14979.
22. Groth C, Hu X, Weber R, Fleming V, Altevogt P, Utikal J, et al. Immunosuppression mediated by myeloid-derived suppressor cells (MDSCs) during tumour progression. *Br J Cancer* 2019;**120**:16−25.
23. Guha P, Gardell J, Rabinowitz B, Lopes M, DaSilva NA, Rowley D, et al. Monocytic and granulocytic myeloid-derived suppressor cell plasticity and differentiation are organ-specific. *Oncogene* 2021;**40**:693−704.
24. Yang L, Pang Y, Moses HL. TGF-β and immune cells: an important regulatory axis in the tumor microenvironment and progression. *Trends Immunol* 2010;**31**:220−7.
25. Villalba M, Evans SR, Vidal-Vanaclocha F, Calvo A. Role of TGF-β in metastatic colon cancer: it is finally time for targeted therapy. *Cell Tissue Res* 2017;**370**:29−39.
26. Trapani JA. The dual adverse effects of TGF-β secretion on tumor progression. *Cancer Cell* 2005;**8**:349−50.
27. Palomares O, Akdis M, Martin-Fontecha M, Akdis CA. Mechanisms of immune regulation in allergic diseases: the role of regulatory T and B cells. *Immunol Rev* 2017;**278**:219−36.
28. Xu L, Kitani A, Strober W. Molecular mechanisms regulating TGF-beta-induced Foxp3 expression. *Mucosal Immunol* 2010;**3**:230−8.
29. Sanjabi S, Oh SA, Li MO. Regulation of the immune response by TGF-beta: from conception to autoimmunity and infection. *Cold Spring Harbor Perspect Biol* 2017;**9**:a022236.
30. Lodyga M, Hinz B. TGF-β1-A truly transforming growth factor in fibrosis and immunity. *Semin Cell Dev Biol* 2020;**101**:123−39.
31. Huang CY, Chung CL, Hu TH, Chen JJ, Liu PF, Chen CL. Recent progress in TGF-beta inhibitors for cancer therapy. *Biomed Pharmacother* 2021;**134**:111046.
32. Principe DR, Underwood PW, Kumar S, Timbers KE, Koch RM, Trevino JG, et al. Loss of SMAD4 is associated with poor tumor immunogenicity and reduced PD-L1 expression in pancreatic cancer. *Front Oncol* 2022;**12**:806963.
33. Slot JW, Geuze HJ. Cryosectioning and immunolabeling. *Nat Protoc* 2007;**2**:2480−91.
34. Summersgill B, Clark J, Shipley J. Fluorescence and chromogenic *in situ* hybridization to detect genetic aberrations in formalin-fixed paraffin embedded material, including tissue microarrays. *Nat Protoc* 2008;**3**:220−34.
35. Upadhya R, Madhu LN, Attaluri S, Goes Gitai DL, Pinson MR, Kodali M, et al. Extracellular vesicles from human iPSC-derived neural stem cells: miRNA and protein signatures, and anti-inflammatory and neurogenic properties. *J Extracell Vesicles* 2020;**9**:1809064.
36. Siegel PM, Massagué J. Cytostatic and apoptotic actions of TGF-beta in homeostasis and cancer. *Nat Rev Cancer* 2003;**3**:807−21.
37. Had ija MP, Kapitanović S, Radosević S, Cacev T, Mirt M, Kovacević D, et al. Loss of heterozygosity of DPC4 tumor suppressor gene in human sporadic colon cancer. *J Mol Med (Berl)* 2001;**79**:128−32.
38. Yamamoto T, Kawada K, Itatani Y, Inamoto S, Okamura R, Iwamoto M, et al. Loss of SMAD4 promotes lung metastasis of colorectal cancer by accumulation of CCR1$^+$ tumor-associated neutrophils through CCL15−CCR1 axis. *Clin Cancer Res* 2017;**23**:833−44.
39. Terabe M, Matsui S, Park JM, Mamura M, Noben-Trauth N, Donaldson DD, et al. Transforming growth factor-β production and myeloid cells are an effector mechanism through which CD1d-restricted T cells block cytotoxic T lymphocyte-mediated tumor immunosurveillance: abrogation prevents tumor recurrence. *J Exp Med* 2003;**198**:1741−52.
40. Lavie D, Ben-Shmuel A, Erez N, Scherz-Shouval R. Cancer-associated fibroblasts in the single-cell era. *Nat Can (Ott)* 2022;**3**:793−807.
41. Derynck R, Turley SJ, Akhurst RJ. TGFβ biology in cancer progression and immunotherapy. *Nat Rev Clin Oncol* 2021;**18**:9−34.
42. Derynck R, Jarrett JA, Chen EY, Eaton DH, Bell JR, Assoian RK, et al. Human transforming growth factor-beta complementary DNA sequence and expression in normal and transformed cells. *Nature* 1985;**316**:701−5.
43. Zhou L, McMahon C, Bhagat T, Alencar C, Yu Y, Fazzari M, et al. Reduced SMAD7 leads to overactivation of TGF-beta signaling in MDS that can be reversed by a specific inhibitor of TGF-beta receptor I kinase. *Cancer Res* 2011;**71**:955−63.
44. Fridlender ZG, Sun J, Kim S, Kapoor V, Cheng G, Ling L, et al. Polarization of tumor-associated neutrophil phenotype by TGF-beta: "N1" *versus* "N2" TAN. *Cancer Cell* 2009;**16**:183−94.
45. Gabrilovich DI, Ostrand-Rosenberg S, Bronte V. Coordinated regulation of myeloid cells by tumours. *Nat Rev Immunol* 2012;**12**:253−68.
46. Liu S, Wu X, Chandra S, Lyon C, Ning B, Jiang L, et al. Extracellular vesicles: emerging tools as therapeutic agent carriers. *Acta Pharm Sin B* 2022;**12**:3822−42.
47. Xu Y, Xiong J, Sun X, Gao H. Targeted nanomedicines remodeling immunosuppressive tumor microenvironment for enhanced cancer immunotherapy. *Acta Pharm Sin B* 2022;**12**:4327−47.
48. Vaidehi N, Schlyer S, Trabanino RJ, Floriano WB, Abrol R, Sharma S, et al. Predictions of CCR1 chemokine receptor structure and BX 471 antagonist binding followed by experimental validation. *J Biol Chem* 2006;**281**:27613−20.
49. Derynck R, Budi EH. Specificity, versatility, and control of TGF-β family signaling. *Sci Signal* 2019;**12**:eaav5183.
50. Derynck R, Zhang YE. Smad-dependent and Smad-independent pathways in TGF-β family signalling. *Nature* 2003;**425**:577−84.
51. Mariathasan S, Turley SJ, Nickles D, Castiglioni A, Yuen K, Wang Y, et al. TGFβ attenuates tumour response to PD-L1 blockade by contributing to exclusion of T cells. *Nature* 2018;**554**:544−8.
52. Kinker GS, Vitiello GAF, Diniz AB, Cabral-Piccin MP, Pereira PHB, Carvalho MLR, et al. Mature tertiary lymphoid structures are key niches of tumour-specific immune responses in pancreatic ductal adenocarcinomas. *Gut* 2023;**72**:1927−41.
53. Horeweg N, Workel HH, Loiero D, Church DN, Vermij L, Léon-Castillo A, et al. Tertiary lymphoid structures critical for prognosis in endometrial cancer patients. *Nat Commun* 2022;**13**:1373.
54. Paijens ST, Vledder A, de Bruyn M, Nijman HW. Tumor-infiltrating lymphocytes in the immunotherapy era. *Cell Mol Immunol* 2020;**18**:842−59.
55. Schumacher TN, Thommen DS. Tertiary lymphoid structures in cancer. *Science* 2022;**375**:39.
56. Castiglioni A, Yang Y, Williams K, Gogineni A, Lane RS, Wang AW, et al. Combined PD-L1/TGFβ blockade allows expansion and differentiation of stem cell-like CD8 T cells in immune excluded tumors. *Nat Commun* 2023;**14**:4703.
57. Lind H, Gameiro SR, Jochems C, Donahue RN, Strauss J, Gulley JL, et al. Dual targeting of TGF-β and PD-L1 *via* a bifunctional anti-PD-

L1/TGF-βRII agent: status of preclinical and clinical advances. *J Immunother Cancer* 2020;**8**:e000433.
58. Yi M, Zhang J, Li A, Niu M, Yan Y, Jiao Y, et al. The construction, expression, and enhanced anti-tumor activity of YM101: a bispecific antibody simultaneously targeting TGF-β and PD-L1. *J Hematol Oncol* 2021;**14**:27.
59. Zhang D, Wu T, Qin X, Qiao Q, Shang L, Song Q, et al. Intracellularly generated immunological gold nanoparticles for combinatorial photothermal therapy and immunotherapy against tumor. *Nano Lett* 2019;**19**:6635−46.
60. Wu T, Qi Y, Zhang D, Song Q, Yang C, Hu X, et al. Bone marrow dendritic cells derived microvesicles for combinational immunochemotherapy against tumor. *Adv Funct Mater* 2017;**27**:1703191.
61. Qin X, Yang C, Xu H, Zhang R, Zhang D, Tu J, et al. Cell-derived biogenetic gold nanoparticles for sensitizing radiotherapy and boosting immune response against cancer. *Small* 2021;**17**:2103984.
62. Sautès-Fridman C, Petitprez F, Calderaro J, Fridman WH. Tertiary lymphoid structures in the era of cancer immunotherapy. *Nat Rev Cancer* 2019;**19**:307−25.